SMC complex unidirectionally translocates DNA by coupling segment capture with an asymmetric kleisin path

Masataka Yamauchi[1], Giovanni B. Brandani[1], Tsuyoshi Terakawa[1], and Shoji Takada[1]*

[1] Department of Biophysics, Graduate School of Science, Kyoto University, Kitashirakawa-Oiwakecho, Sakyo-ku, 606-8502, Kyoto, Japan

* To whom correspondence should be addressed. Tel: (+81)75-753-4220; Fax: (+81)75-753-4222; Email: takada@biophys.kyoto-u.ac.jp

ABSTRACT

SMC (structural maintenance of chromosomes) protein complexes are ring-shaped molecular motors essential for genome folding. Despite recent progress, the detailed molecular mechanism of DNA translocation in concert with the ATP-driven conformational changes of the complex remains to be clarified. In this study, we elucidated the mechanisms of SMC action on DNA using multiscale molecular dynamics simulations. We first created a near-atomic full-length model of prokaryotic SMC-kleisin complex that implemented protein-DNA hydrogen bond interactions derived from fully atomistic simulations and emulated ATP-dependent conformational changes. Extensive simulations of the SMC complex with 800 base pairs of duplex DNA over the ATP cycle revealed unidirectional DNA translocation via the DNA segment capture mechanism. The process exhibited a step size of ~200 base pairs, wherein the complex captured a DNA segment of about the same size within the SMC ring in the engaged state, followed by its pumping into the kleisin ring as ATP was hydrolyzed. We found that the hinge-DNA interaction is not critical for the DNA translocation. On the other hand, analysis of trajectories identified the asymmetric path of the kleisin as a critical factor for the observed unidirectionality.

SIGNIFICANCE STATEMENT

Ring-shaped SMC (structural maintenance of chromosomes) protein complexes, which are highly conserved across all three domains of life, play an essential role in chromosome organization through a process called DNA loop extrusion. However, the molecular mechanism underlying the ATP-dependent motor activity of SMC complexes remains unclear. Using all-atom and residue-resolution coarse-grained molecular dynamics simulations, we revealed that prokaryotic SMC complexes translocate unidirectionally along DNA via a segment capture mechanism. We found that the unidirectionality arises from the kleisin subunit breaking the symmetry of the ring-shaped SMC complex structure. Our findings provide insights into the molecular motor mechanisms shared by SMC complexes.

INTRODUCTION

The structural maintenance of chromosomes (SMC) are protein complexes essential to organize chromosome structures and are highly conserved across the three domains of life (1–5). Eukaryotic SMCs include condensin, which plays a significant role in mitotic chromosome architecture; cohesin, known for its dual roles in sister chromatid cohesion and chromosome folding during interphase; and SMC5/6, implicated in DNA damage repair, chromosome segregation, and replication processes (6). Bacteria and archaea also possess SMC complexes whose architecture resembles their eukaryotic counterparts (7).

All SMC complexes have a common ring-shaped architecture of two structured SMC subunits and a kleisin subunit, which is mainly disordered (1, 5). Each SMC subunit has an ATPase head domain and a hinge domain, which are connected by a ~50nm coiled-coil arm. Two SMC chains dimerize through their hinge domains, while the kleisin bridges the two ATPase head moieties by binding through its N- and C-termini, thus forming a closed ring. Eukaryotic SMC chains form heterodimers, SMC1 and SMC3 for cohesin, SMC2 and SMC4 for condensin, and SMC5 and SMC6 for the SMC5/6 complex, while the prokaryotic ones form homodimers. Other non-SMC subunits, KITE (kleisin-interacting tandem winged-helix element) and HAWK (HEAT repeat proteins associated with kleisins), can be further recruited onto the kleisin subunit.

SMC proteins are also characterized by conformational changes coupled with the ATP hydrolysis cycle (1–5). In the ATP-bound state (designated as the engaged state hereafter), two ATPase heads are engaged to form a dimer to catalyze ATP hydrolysis. The two coiled-coil arms separately emanate from the engaged heads and converge at the hinge domains, forming an O-shaped ring structure. In the engaged state, a second ring is formed by the kleisin as it links together the head domains of each SMC through its intrinsically disordered region. After ATP hydrolysis, the two head domains dissociate, with the coiled-coil arms forming a V-shaped structure (designated as the V-shape state). In the nucleotide-free state, the two ATPase heads associate again, but differently from the engaged state, in which two coiled-coil arms become aligned in parallel, forming an I-shaped structure (designated as the disengaged state). Notably, throughout the hydrolysis cycle, the kleisin subunit keeps bridging two ATPase head moieties, maintaining the overall loop topology.

These ATP-dependent conformational changes have been suggested to realize the SMC motor activities responsible for higher-order chromosome organization (8–12). Direct evidence that SMC complexes act as ATP-dependent molecular motors was first obtained from single-molecule imaging studies on budding yeast condensin (13), revealing its unidirectional translocation along DNA. Single-molecule imaging studies later demonstrated DNA loop extrusion by condensin (14), cohesin (15, 16), and SMC5/6 complexes (17). Time-resolved Hi-C and ChiP-seq experiments also provided evidence of ATP-dependent translocation activity of bacterial SMC complexes (18, 19).

While the ATP-dependent conformational changes and biochemical activities of SMC complexes have been characterized, the link between the two remains elusive, with several models proposed to delineate the molecular mechanism of DNA translocation and loop extrusion (2–4). The “DNA-segment capture” model (20–22) was originally inspired by the structural features of prokaryotic SMC complexes: the I-shaped conformation in the apo state and open-ring conformation in the ATP-bound state. In this model, DNA loop extrusion is achieved by translocating along DNA while anchoring it at an additional binding site, presumably through a safety belt (23). This DNA-segment capture model has been extended to eukaryotic SMC complexes. DNA entrapment in the kleisin and two SMC sub-compartments, consistent with the segment capture mode, was experimentally demonstrated for the SMC5/6 holo-complex (24). In contrast, a revised “hold-and-feed” model was proposed to explain observations on condensin (25). For the DNA loop extrusion mechanism of condensin and cohesin, the “scrunching” (26, 27), “swing-and-clamp” (28), and “Brownian ratchet” (29) models, which emphasize the folding of the coiled-coil arms at the elbow joints, have also been proposed. However, the detailed mechanism by which the ATP-dependent conformational changes of the SMC complexes are coupled with DNA translocation has not yet been thoroughly tested.

In this study, we aimed to understanding the molecular mechanism of DNA translocation by an SMC complex using molecular dynamics (MD) simulations. In contrast to previous work (22, 30, 31), we employed a bottom-up multiscale approach where dynamics arise from the fundamental physical interactions of the system. While ATP-dependent cyclic conformational changes of the SMC complexes were encoded based on experimental structural knowledge, DNA dynamics is purely derived from physical interaction with the SMC complexes in unbiased manner without assuming

any specific DNA translocation model *a priori*. As a relatively simple model system broadly representative of SMC complexes, we focused on prokaryotic SMC, which is made of the SMC homodimer and the kleisin subunit, ScpA.

We first performed fully atomistic MD simulations with explicit water solvent to uncover fundamental hydrogen bond interactions between SMC and duplex DNA. Next, we conducted coarse-grained MD simulations using a rigorous physics-based modeling approach at near-atomic resolution, realizing the cyclic conformational changes occurring in the full-length SMC-ScpA complex throughout ATP binding and hydrolysis. We then characterized the key DNA-binding sites in the SMC complex through simulations in the presence of DNA, incorporating long-ranged Coulombic interactions based on the Debye-Hückel approximation and short-ranged hydrogen bonds based on the atomistic MD simulations. Finally, we performed extensive simulations where the SMC complex undergoes cyclic conformational changes as an 800 base pairs (bp) long DNA molecule is loaded inside the SMC complex, successfully observing unidirectional DNA translocation. Analysis of our MD trajectories reveals that translocation proceeds via DNA segment capture within the SMC ring and its subsequent pumping to the kleisin ring, with the asymmetric path of the kleisin being responsible for the unidirectionality. We also analyzed many non-productive trajectories to discuss the inherent difficulty of efficient DNA translocation.

RESULTS

Interactions between prokaryotic SMC ATPase heads and DNA

Recent cryo-EM structures have uncovered highly conserved DNA-clamping states among SMC complexes (32–36), suggesting that DNA binding to the upper surface of the ATPase heads is crucial for SMC functionality. As prokaryotic SMC ATPase-DNA complexes have not been experimentally resolved at high resolution, we first studied this system using all-atom MD simulations. The simulations allowed us to identify the hydrogen bonds formed between DNA and key basic residues on SMC and to incorporate these interactions (37) into coarse-grained simulations for the following stages of our investigation. Based on the available biochemical evidence (38), we prepared an initial structure by placing a 47 bp duplex DNA fragment on the upper surface of engaged *Pyrococcus furiosus* (*Pf*) SMC ATPase heads (PDB code: 1xex) (39) and conducted five independent 1μs-long simulations (refer to Methods for more

details). Starting from its initially straight conformation, the DNA adopted moderately bent conformations as the bending increased DNA interactions with the head domains (Fig. 1A upper panel and Movie S1 for a representative trajectory). DNA binding to the top head surface remained stable for the entire simulation in four out of five trajectories. In one case, one DNA end detached from the heads in the middle of the simulation, losing most interactions on that side, so this trajectory was excluded from the subsequent interaction analysis.

During our trajectories, the SMC ATPase heads gradually formed hydrogen bonds with the DNA backbone, reaching an equilibrium with 13 ± 3 bonds on average after ~500 ns (Fig. 1A lower panel, and Fig. S1). In subsequent analyses, we focused on the data after 500 ns. Figure 1B shows the probability of hydrogen-bond formation, highlighting many critical residues on the top head surface stabilizing the interaction with DNA (Fig. 1C, right panel). In particular, basic residues Arg120, Arg123, Arg111, Arg62, and Lys56 frequently formed hydrogen bonds (Figs. 1B and 1C, left panel). The critical role of these residues is consistent with previous experiments by Vazquez-Nunez et al. demonstrating that the triple alanine mutations of Lys60, Arg120, and Lys122 in *Bacillus subtilis* (*Bs*) SMC (which correspond to Arg62, Arg120, and Arg123 in *Pf*SMC) result in impaired DNA binding ability and a severe growth phenotype (38). We will later use these findings to optimize the representation of protein-DNA interactions in our residue-resolution model of ATP-dependent DNA translocation.

Modelling the full-length SMC-ScpA complex in the disengaged form

Next, we turn to the problem of modeling the full-length prokaryotic SMC complex (40, 41). A previous biochemical study showed that in several archaea, such as *Pyrococcus yayanosii* (*Py*), a binary complex (SMC-ScpA) is more likely to form than a tripartite complex (SMC-ScpAB) due to the absence of the ScpB (KITE) binding segment in the ScpA subunit (42). Therefore, our current study focuses on the SMC-ScpA binary complex as a minimal configuration to investigate the translocation of SMC complexes.

To prepare the initial configuration for our MD simulations, we built a full-length model of SMC-ScpA in the disengaged (I-shaped) form. We considered the full-length *Py*SMC homodimer model (Fig. S2A), which was previously constructed based on protein cross-linking experiments and crystal structures of individual domains (20), as a reference structure. We added the ScpA subunit to this model using Modeller 10.1

(43). Here, crystal structures (PDB codes: 3zgx and 5xns) and an AlphaFold2 predicted complex structure were used as templates, which comprises the ScpA N-terminal domain (NTD) and C-terminal domain (CTD) bound to the SMC ATPase head domain (Fig. S2B-S2D). Details are provided in the Methods section. The resulting full-length model of SMC-ScpA in the disengaged form is shown in Fig. S2E. Our modeling generated the expected ring topology via the binding of the ScpA NTD to one SMC subunit and the ScpA CTD to the other. We note that while SMC forms a homodimer, the binding to ScpA breaks the original symmetry of the structure. For convenience, hereafter, we distinguish the two subunits by color; the blue subunit interacts with NTD, while the red subunit interacts with CTD of ScpA.

MD simulations of SMC-ScpA ATP-dependent conformational changes

During ATP hydrolysis, the SMC complex undergoes cyclic conformational changes as it transitions among three nucleotide-binding states: Apo (disengaged), ATP-bound (engaged), and ADP-bound (V-shape) states (5, 44). Due to the complex molecular size (over 2000 amino acid residues and ~50 nm-long coiled-coils) and large-scale motions involved, all-atom MD simulations are computationally too costly to observe these conformational changes. To overcome this issue, we employed the structure-based AICG2+ coarse-grained model at residue resolution (45), where each amino acid in proteins is represented by one bead located on the Cα atom. The combination of this protein model and the 3SPN.2C model for DNA has been successfully applied to investigate many protein-DNA complexes (46–50).

Using this model, we can effectively emulate the ATP-dependent conformational changes in the SMC complex by switching the reference structures in the model (51). The choice of reference structure in each ATP state is not arbitrary but is instead based on independent experimental observations established in past structural studies on SMC complexes. For the disengaged state, the reference structure of the full-length SMC-ScpA is the one we have built above. For the engaged state, we changed the reference structure of the ATPase heads to that of the corresponding crystal structure of *Pf*SMC (PDB code: 1xex, Fig. S2F). For the V-shape structure, we used the same reference structure as the disengaged one, except we turned off the inter-subunit interactions between the ATPase head domains, as these are not expected to be stably interacting in this state (44, 52–54). During the MD simulations, the potential energy function was switched in the following order:

disengaged, engaged, V-shape, and disengaged, with each state lasting for 5×10^7 MD steps.

Figure 2 and Movie S2 show a representative trajectory illustrating the ATP-dependent conformational changes of the SMC-ScpA complex. In the initial disengaged state, the entire SMC complex adopted the I-shaped structure where two ATPase heads were in contact, and the coiled-coil arms were aligned in parallel (Fig. 2A). Upon transition to the engaged state, the two ATPase heads were quickly rearranged to form the new inter-subunit contacts. The fractions of formed contacts, Q-scores, that exist at the disengaged (engaged) states quickly decreased (increased) (Fig. 2A, top two plots). The head dimer rearrangement induced the opening of the adjacent coiled-coil arms, which further propagated to open the hinge domain, as monitored by the hinge angle (Fig. 2A, bottom plot). The resulting configuration was an O-shaped structure. The two ATPase heads dissociated in the subsequent V-shape state, while the dimerized hinge domain maintained an open hinge conformation (Fig. 2A, bottom two plots). Finally, the SMC-ScpA complex returned to the disengaged conformation upon re-establishing the inter-subunit interactions between the ATPase head domains. Fig. 2B shows the average distances between intermolecular amino acid residues to characterize typical conformations in each nucleotide state. This is computed from the distance between a Cα atom of *i*-th residue for the first SMC protein and a Cα atom of *i*-th residue for the second SMC protein. The results clearly represent that the disengaged state has a rod-shaped structure, the engaged state has an open-ring structure, and the V-shape state has a dissociated ATPase heads and a dimerized hinge domain. These structural features are consistent with experimental observations by electron micrographs (44, 54)

DNA binding sites in the SMC-ScpA complex

The DNA binding sites on the SMC complex are expected to play critical roles in DNA translocation and loop extrusion, but these were not comprehensively investigated for prokaryotic SMC. Here, we characterize DNA binding in the full-length SMC-ScpA complex using residue-resolution MD simulations, a similar approach previously employed for yeast condensin (55).

To set the initial structures for the DNA binding simulations, we distributed five 40 bp double-strand (ds) DNAs with identical random sequences as used in prior

fluorescence anisotropy measurements (38) around the engaged SMC-ScpA complex. The DNA was modeled using the 3SPN2.C coarse-grained model (56), where each nucleotide was represented by three beads, each located at the base, sugar, and phosphate groups. Protein and DNA interact through excluded volume, Debye-Hückel electrostatics, and an effective model of hydrogen bond interactions (37) with parameters obtained from the previous all-atom MD simulations (more details are provided in the Methods section). We conducted 100 simulation runs of 5×10^7 steps, each starting from a different initial distribution of DNA molecules, all at 150 mM monovalent ion concentration (Simulations at 300 mM did not change major binding sites although the bindings were weakened as expected).

Figures 3A and 3B show the DNA contact probabilities as a function of SMC residue. The analysis revealed three major DNA binding sites on the SMC heads, coiled-coil arms, and hinge domain. The ScpA subunit also possesses a DNA-binding patch in its disordered region due to the consecutive arrangement of positively charged lysine residues (at positions 126-130). Figure 3C illustrates a representative snapshot of DNAs that bound to the SMC-ScpA complex; here, DNA was observed to be sandwiched between the coiled-coil arms on the inner side of the hinge, consistent with previous biochemical experiments (38, 53, 57, 58). The DNA also binds to the top surface of ATPase heads, which aligns with our all-atom simulations and previous biochemical experiments (38). Figures 3D-H illustrate a typical DNA binding event on the top surface of ATPase heads: DNA initially bound to the side surface of the heads (Figs. 3E and F) and subsequently migrated to the top surface (Figs. 3G and H) driven by the formation of hydrogen bonds (Fig. 3D, bottom plot). It is worth noting that disabling hydrogen-bond interactions resulted in DNA remaining attached to the side surface of the ATPase heads (Fig. S3). This highlights the importance of hydrogen bonds in accurate modeling of the DNA-head binding, as long-range electrostatic interactions alone were insufficient.

DNA translocation via DNA-segment capture

We employed the established full-length SMC-ScpA model to address how the SMC complex couples ATP-dependent conformational changes with DNA binding to realize unidirectional SMC translocation. To this end, we conducted the same cyclic conformational change simulations of SMC-ScpA with a long (800bp) dsDNA topologically threaded into the ring complex. We started our simulations in the

disengaged state with DNA placed into the kleisin ring (Fig. S4) (38), switched to the engaged, then V-shape, and again disengaged state. In the production simulations, we performed 50 individual simulations for the first disengaged and subsequent engaged state. Due to its stochastic nature, for subsequent V-shape and disengaged states, we repeated multiple simulations for each selected final structure with different realizations of fluctuating forces; consequently, the number of trajectories increased to 190 and 770 for the V-shape and the last disengaged state, respectively, allowing us to explore the key processes. Here, the monovalent ion concentration was set to 300 mM to weaken the electrostatic interactions between the SMC complex and DNA and accelerate DNA dynamics.

Figures 4A-D, 4I, S5, and Movie S4 illustrate one trajectory exhibiting DNA translocation by the SMC complex through one entire ATP hydrolysis cycle. In the initial disengaged state (Fig. 4A), the coiled-coil arms and ATPase head domains were juxtaposed throughout the entire 1×10^8 MD steps within this state, while the DNA remained entrapped in the kleisin ring. Switching the reference potential to that of the engaged state due to ATP binding rapidly induced the transition of the SMC conformation. After some lag time, we observed a gradual tilting of DNA along the side surface of the ATPase heads (Fig. 4B left); then, as DNA progressively formed hydrogen bonds to the top surface of the ATPase heads during the time from 1×10^8 to 3×10^8 MD steps, a downstream segment of DNA was captured into the hinge on the opposite side of the SMC complex (Fig. 4B right and 4I), as predicted by the segment capture model. This process formed a DNA loop structure that was stabilized on one end by binding to the SMC heads and on the other by binding to the hinge. In the subsequent V-shape state adopted upon ATP hydrolysis, the SMC complex maintained the DNA loop structure within the SMC ring (Fig. 4C). While the ATPase heads and kleisin kept their contact with DNA, the DNA occasionally detached from the hinge domain due to the weak binding affinity. Transitioning from the V-shape to disengaged states upon ADP unbinding (Fig 4D), the DNA was pushed from the hinge domain towards the kleisin ring as the SMC complex closed its coiled-coil arms. The DNA segment initially bound to the kleisin ring detached, and the opposite DNA segment pumped from the hinge domain was instead entrapped in the kleisin ring. Consequently, the SMC complex achieved the DNA translocation, returning to its original configuration but with the DNA shifted by the size of the loop entrapped during segment capture.

The average and standard deviation of the step size observed in the successful translocation was 216 ± 71 bp (ranging from 42 bp to 356 bp, Fig. 4K, Fig. S7), close to the length of the DNA loop captured in the engaged state, 206 ± 30 bp (Fig. 4L). The variation of step size and the occasional discrepancy between the step and loop sizes originates from the sliding of DNA around the ATPase heads, hinge, and coiled-coil arms through the ATP-hydrolysis cycle.

Notably, Figs. 4E-H, 4J, S6, and Movie S5 demonstrate that the SMC complex can translocate along DNA even when the SMC hinge did not capture DNA in the engaged state (Fig. 4F, right). The step size observed in this process was 225 ± 82 bp (Fig. S8, right), which was compatible to the step size of 207 ± 58 bp when the DNA reached the hinge domain (Fig. S8, left). This indicates that DNA binding to the hinge domain is not essential for translocation as long as the DNA loop is captured within the SMC ring, explaining previous findings (22, 38, 59).

Zipping motion of coiled-coil arms pushes the DNA from hinge domain toward kleisin ring

In the translocating trajectories, DNA consistently moved from the hinge domain toward the kleisin ring in the final disengaged state (Figs. 4D and 4H), never moving backward from the ATPase heads to the hinge domain. To elucidate the molecular mechanism underlying this phenomenon, we explored the molecular dynamics of the coiled-coil arms when the SMC complex transitions from the V-shape to the disengaged state. Figures 4M and S9 illustrate the intermolecular Q-scores for the coiled-coil arms and the ATPase head domains. The coiled-coil arms closed sequentially, initially forming intermolecular contacts at the hinge side, followed by the middle, and finally at the ATPase head side and between the ATPase head domains (Movie S6). Therefore, the zipping-up of the coiled-coil arm consistently occurs sequentially from the hinge to the ATPase head domains, facilitating the unidirectional pushing of the captured DNA segment from the hinge toward the ATPase heads.

DNA can be slipped or trapped in the coiled-coil arm during the cycle

In the above simulations, the motions of DNA during the cyclic conformational change in SMC-ScpA were highly stochastic. Only fractions of the runs (45 of 770 runs) exhibited DNA translocation, so we investigated the conditions required for productive translocation. We summarized the range of observed DNA dynamics in Fig. 5. First,

during the simulations in the disengaged state, the system displayed highly similar behavior across all 50 runs: DNA remained in the kleisin ring with some unbiased diffusion (Figs. 5AB). During the transition from disengaged to engaged state, the DNA bound to the top surface of the ATPase heads via hydrogen bonds, and a DNA segment was captured within the SMC ring in 8 of 50 runs (Fig. 5C, middle). The DNA reached the hinge domain in one of the eight runs, while DNA did not reach the hinge domain in the remaining seven runs. In some other trajectories, the SMC heads did not reach the engaged form, possibly inhibited by DNA interacting with the head domains on the side interfaces (23/50 runs) (Fig. 5C, left). We also observed many runs in which DNA was not caught by the top surface of the ATPase heads at the end of runs (19/50 runs), and thus, the DNA loop was not formed (Fig. 5C right). These final structures that did not capture DNA segments resemble intermediate states of the successful DNA capture pathways, indicating this is mainly due to the limited simulation time.

We simulated the transition to the V-shape state from the snapshot in which a DNA segment was captured. The DNA loop captured within the SMC ring mainly remained unchanged in 77 of 190 runs (Fig. 5D, right), while in the remaining, it disappeared due to DNA slippage. The fundamental cause of slippage was the destabilization of the interactions between DNA and the top surface of the SMC heads upon ATP hydrolysis, as hydrogen bonds were excluded from the model due to the dissociation of the head domain dimer in the V-shape state. The DNA that was interacting with the top interface of the ATPase heads moved to the patch on the side interface of the ATPase heads. The dissociation of the two ATPase heads further destabilized the interaction with DNA, leading to DNA sliding along the hinge and coiled-coil arms, ultimately destabilizing the DNA loop. The release of the DNA loop leads to an overall configuration similar to that before the DNA segment capture. DNA slippage could also occur in actual SMC complexes, although its probability may depend on the specific SMC and system conditions.

Starting from the structures that maintained the DNA loop in the above simulations, we conducted MD simulation to the subsequent disengaged state. In 45 of 770 runs, the captured DNA segment in the SMC ring was pumped down toward the kleisin by the zipping of the coiled-coil arms, resulting in successful DNA translocation (Fig. 5E, right). In 349 cases, the DNA loop disappeared, and the kleisin kept binding to DNA close to the original site, similar to the DNA slippage described

above (Fig. 5E, left). We also observed trajectories where the DNA remained trapped in the middle of the coiled-coil arms during its motion from the hinge to the kleisin (Fig. 5E, the second from the left, 375 cases). This was caused by the high strength of the interactions between the coiled-coil arms in the disengaged state, which suggests that repeated opening and closing of the coiled-coil arms is required to avoid trapping.

We finally investigated the dependence of the success rate of translocation as a function of the size of the captured DNA loop formed at the end of the engaged state. The length of the DNA loop for trajectories resulting in translocation was 206 ± 30 bp (Fig. 4L). In contrast, the loop length for trajectories not resulting in translocation was shorter, measuring 138 ± 29 bp (Fig. 4L), suggesting the existence of a critical loop size required for translocation. The time series analysis of the captured DNA length (Fig. S10) indicated that a DNA loop consisting of ~100 bp tends to be formed as an intermediate state. Since the trajectories not leading to translocation were trapped in this state, more extended simulations may be necessary to form a sufficiently large loop for translocation.

Asymmetric kleisin path makes unidirectionality of SMC translocation

In the above simulations, we consistently observed DNA translocations by the SMC complex in the same direction along the DNA molecule. Unidirectionality of DNA translocation requires breaking the symmetry of the SMC-ScpA complex. Since prokaryotic SMC proteins form a homodimer, this can only be ensured by binding to the ScpA subunit. Specifically, the ScpA NTD binds to the coiled-coil region close to the head in one SMC subunit (in blue in Fig. S2), while the ScpA CTD binds to the bottom side of the head in the other SMC subunit (in red), imposing the symmetry breaking.

Figure 6A shows typical snapshots of when the SMC-ScpA complex captured a DNA segment within its ring structure in the engaged state. The DNA loop was always inserted into the SMC ring from the side where the ScpA was located in all successful segment-capture trajectories. This result led to the hypothesis that the path of ScpA (kleisin) determined the direction of translocation (Fig. 6B). In this model, we considered two possible paths of the kleisin ring relative to the ATPase heads: the front side path and the backside path. When the kleisin traverses in front of the heads, topological constraints require a DNA loop inserted from the front side of the SMC complex (Fig. 6B, upper left). Upon completion of SMC translocation, the DNA

segment marked in orange escapes from the complex. In contrast, the segment marked in green is pumped from the hinge domain to the kleisin ring and entrapped there, resulting in the SMC translocation from left to right relative to the DNA (Fig. 6B, upper right). On the other hand, when the kleisin traverses behind the ATPase heads, a DNA loop forms on the front side (Fig. 6B, lower left), resulting in the SMC translocation from right to left relative to the DNA (Fig. 6B, lower right). Thus, the kleisin path determines the direction of SMC translocation, and unidirectional SMC translocation occurs if the kleisin path is restrained on one side.

To reveal whether the path of kleisin exhibits a bias, we computed the spatial distribution of the center of mass of the ScpA DNA-binding patch (K126-K130) relative to the SMC heads in the engaged state (Fig. 6C, left), finding this was indeed restrained exclusively to one side. This ScpA location was consistent with the side where the DNA loop was inserted into the SMC ring, as seen in Fig. 6A. To rule out the possibility that the biased positioning of ScpA was a result of DNA-kleisin interaction, we further analyzed the spatial distribution of ScpA in the absence of DNA, finding a similar positional bias (Fig. 6C, middle). In other words, kleisin binding restrains its configuration to a specific side of the SMC heads. This restraint was in part due to the short length of the disordered region of ScpA, consisting of 63 residues (residues 82-144 of ScpA), which structurally impedes reaching the backside, and in part to the peptide chains of ScpA emanating toward only one side of the SMC at their interface with the complex as they bind to the two SMC subunits. In summary, we revealed that the asymmetric ScpA path is the critical determinant of the SMC unidirectional DNA translocation via a DNA segment capture.

DISCUSSION

DNA segment capture as the mechanism of the DNA translocation by SMC complexes

DNA translocation and loop extrusion by SMC complex have been hypothesized to be the fundamental mechanisms for chromosome compaction and the formation of topologically associating domains (8–12). Progress has been made in the past decade toward elucidating the molecular mechanisms behind the motor activity of the SMC protein (2–4). However, the relationship between ATP-dependent conformational changes occurring in SMC complexes and translocation along DNA has not been fully

understood, and the proposed mechanisms (2–4) have yet to be thoroughly tested at the molecular level.

In this study, we conducted all-atom and residue-resolution MD simulations to elucidate the molecular mechanism underlying DNA translocation by SMC complexes. To simplify the system, this study examined the prokaryotic SMC complex consisting of the SMC homodimer and kleisin molecule ScpA. Notably, we employed a bottom-up modeling approach, allowing the mechanism of SMC action to emerge from the simulations without assuming any particular model of DNA translocation. Utilizing structure-based residue-resolution coarse-grained simulations, we successfully reproduced the ATP-dependent cyclic conformational change of the SMC-ScpA complex (Fig. 2). The structural features of SMC complex such as rod-shape in disengaged (Apo) state, open-ring in the engaged (ATP-bound) state, and V-shape-like structure in the V-shape (ADP-bound) state shown in Fig. 2AB are in good agreement with experimental observations by electron micrographs (44). We then identified DNA binding sites at the top of the ATPase heads, the inner side of the hinge, the middle of the coiled-coil arms, and the ScpA disordered region within the full-length SMC complex in the ATP-bound engaged state (Fig. 3). These DNA binding sites agree with the biochemical assays (38, 53, 57). Extensive simulations with a long duplex DNA entrapped in the SMC-ScpA complex throughout cyclic conformational changes revealed that DNA translocation proceeds via the segment capture mechanism: the complex captures a DNA segment in the engaged state to form a DNA loop structure within the SMC ring, and the segment is subsequently pumped toward the kleisin ring, leading to DNA translocation (Fig. 4). We also demonstrated that the hinge-DNA interaction in the engaged state is not necessary for DNA translocation via DNA segment capture.

The step size, the number of DNA base pairs translocated per one ATP cycle, was estimated as 216 ± 71 bp (Fig. 4K). This was largely determined by the length of the DNA loop captured in the engaged state, which is, in turn, affected mainly by the distance between the ATPase heads and the hinge domains. Since the overall SMC architecture and size are well-conserved, a similar step size should also be expected for other SMC complexes. Our results are consistent with a previous simulation study using a coarser mesoscopic model, which suggested a step size of ~180 bp without DNA tension (22). A previous DNA-curtain experiment estimated that yeast condensin translocases along DNA with an average step size of 60 bp (13), which is a lower

bound, as it assumes that all ATP hydrolysis events lead to productive translocation. Magnetic tweezer experiments have measured the median step size of yeast condensin during the loop extrusion process to be 20-40 nm, corresponding to 60-200 bp per step, at DNA stretching forces from 1 to 0.2 pN (27). The loop extrusion speed and ATPase rates were also estimated in *in vitro* studies as ~0.5-1 kbp/s and 2ATP/s for condensin (14), cohesin (15, 16), and SMC5/6 (17) and 300-800 bp/s and 1ATP/s for *B. subtilis* (18, 19) and *C. crescentus* (60) SMCs. A theory also estimated loop extrusion speed as ~0.5 kbp/s without tension and maximum of ~1.5 kbp/s with tension (30). These step sizes are somewhat larger than, but still compatible with our estimates.

Recent magnetic tweezer experiments revealed a DNA twist of -0.6 at each DNA-loop-extrusion step for all eukaryotic SMC proteins (61), implying a common DNA-loop extrusion mechanism. While it would be interesting to elucidate the molecular mechanism of the twist, this is challenging due to important differences between the magnetic tweezer experiments and the current coarse-grained simulation setup. First, we addressed DNA translocation by the SMC complex, but not the DNA loop extrusion in this study. A safety belt, which fixes the DNA at a certain location on the complex, may be essential to convert translocation mode to a DNA-loop extrusion mode and generate twists. However, the current simulation model did not incorporate a possible safety belt such as KITE and HAWK subunits. In the simulation, the DNA ends are also free to move, releasing any twist accumulated during SMC activity. The flexibility of the coiled-coil arms may also explain the twist of -0.6 upon completion of the DNA-loop extrusion step. In the current coarse-grained simulation, the coiled-coil arms are modeled based on the reference structure of the rod-shaped SMC complex, potentially making them slightly stiffer than in reality. Therefore, we anticipate that a different simulation setup is necessary to examine a twist change of -0.6 at each DNA-loop-extrusion step.

Folding of the SMC coiled-coils at so-called elbows has been shown in the condensin (62), cohesin (63, 64), and MukBEF (36, 63), with some models suggesting its role in DNA translocation (2–4, 26–29). However, since evidence of elbow folding is absent in prokaryotic SMC (20) (as well as in SMC5/6 (65, 66)), this was not incorporated into our coarse-grained model. Our simulations realized the DNA translocation via DNA segment capture without assuming elbow folding, suggesting elbow folding is not strictly required for SMC activity. The previous mesoscopic

simulation based on the segment capture model (22) showed that making flexible elbows reduces the step size of translocation, implying that elbow folding may hinder rather than facilitate DNA translocation. The “hold-and-feed” mechanism, a revised DNA-segment capture model recently proposed based on experiments (25), also places more emphasis on the motion of DNA through the chambers formed by the kleisin and HAWK subunits, rather than on elbow folding, without strictly ruling out elbow folding motion. Overall, further investigation is necessary to understand the role of elbows in SMC motor mechanisms.

Unidirectionality of DNA translocation and DNA loop extrusion

Our simulations demonstrated unidirectional DNA translocation by the SMC-ScpA complex. The unidirectionality is realized because the ScpA conformation exhibits a one-sided bias relative to the ATPase heads (Fig. 6C), causing the DNA loop to be consistently captured into the SMC ring from the side where the ScpA is located (Fig. 6A). The one-side biased path of ScpA originates from the short length of the ScpA disordered region and the fact that the peptide chains of ScpA emanate toward only one side of the SMC at their interface with the complex as they bind to the two SMC subunits.

Our simulations revealed at the molecular level that the kleisin short length is critical to breaking the left-right symmetry of the prokaryotic SMC homodimer. On the other hand, eukaryotic SMC complexes, including condensin and cohesin, possess longer kleisin subunits that may not efficiently break the symmetry due to their ability to locate both on the front and the back sides of the ATPase heads. Inspired by the DNA-clamping state (32–36), where the KITE and HAWK subunits interact with the SMC ATPase heads from a specific direction, we propose that these subunits may be the key factors to break the left-right symmetry in eukaryotic SMC complexes. The “hold-and-feed” model for condensin’s DNA loop extrusion further supports this hypothesis (25). In this model, A DNA loop is entrapped in two separate kleisin chambers: a chamber created by the kleisin and Ycg1 anchors a DNA segment. In contrast, another chamber created by the Ycs4 and kleisin provides the motor function through a power stroke from one side when the condensin transits from the ATP-free state to the ATP-bound state in gripping conformation. The Ycs4 subunit breaks the left-right symmetry and ensures the unidirectionality of the DNA loop extrusion. Further studies at the molecular level focused on the role of the kleisin and the accessory SMC

subunits will be of great importance to elucidate within a unified view how SMC complexes realize their unidirectionality during DNA translocation and loop extrusion.

Limitations in current simulations

Here, we discuss the limitations and possible future improvements of our model, which is, to our knowledge, the first to reveal the molecular mechanism of DNA translocation by SMC complexes at residue resolution.

First, the time scale that is reachable by the simulations is one of the major limitations. The ATP hydrolysis rates measured for SMC complexes range between 0.1 s^{-1} and 2 s^{-1} (58), orders of magnitude lower than those in typical molecular motors. While mapping our simulation time scale to the real-time is not rigorously decided, 1 MD step is effectively on the order of 1 ps, meaning our simulations cover the sub-millisecond time scale. Thus, in reality, SMC complexes sample a much broader conformational space than we could in the current simulations. Especially, the DNA segment capture in the engaged state was the most time-consuming process in our simulations, and only a limited number of trajectories had sufficient time to fully realize this transition. The trajectories in the engaged state were often trapped in some intermediate state along the DNA capture pathway (Figs. 5C and S10B), inevitably compromising the subsequent DNA translocation steps during the ATP cycle. Therefore, the success rate would most likely increase if we run the simulation long enough. Also, given the ATP hydrolysis rate and the step size per second observed in *in vitro* experiments (58), the success rate of actual DNA segment capture must be higher than the current coarse-grained simulations. In the future, techniques such as Markov state modeling (67, 68) or enhanced sampling methods (69) may be employed to effectively access the dynamics over longer time scales.

Related to the time scale issue, once the coiled-coil arm closed in the disengaged state, it never reopened during our simulations, frequently causing DNA to remain trapped between the coiled-coil arms as DNA was being pushed from the hinge toward the kleisin (Fig. 5E, the second from the left). Longer time scales could alleviate this problem but could also be an artifact derived from our current modeling choices. Modifying the interactions between the coiled-coil arms by calibrating the intermolecular interaction parameter and employing a multiple-basin potential (70)

could enable repeated opening and closing of the arms, potentially improving the success rate of DNA pumping and translocation.

Second, in the current coarse-grained simulations, the efficiency and success rate of translocation could be sensitive to salt concentration, *i.e.,* the strength of electrostatic interaction between SMC and DNA. For example, we observed strong DNA patches on the side surfaces of the SMC ATPase heads (Fig. 3AB). These DNA patches prevent the efficient migration of DNA onto the top of the ATPase heads in the engaged state when the salt concentration is lower, reducing segment capture efficiency. Also, the SMC coiled-coil arms have a DNA patch at its middle region. This DNA patch could trap the DNA at the middle region of the coiled-coil arms when the DNA is pumped from the hinge to the kleisin ring in the last disengaged state when the salt concentration is lower. For this reason, this study used an ion concentration of 300 mM in the translocation simulations to accelerate DNA dynamics. It is worth mentioning that *Pyrococcus yayanosii*, the prokaryote used in this study, is grown under 2.5–5.5% (w/v) NaCl conditions (optimum 3.5 %), which corresponds to ion concentrations of 420–940 mM (optimum 590 mM) (71). Therefore, the 300 mM ion concentration in the translocation simulations is more physiologically relevant than the standard physiological 150 mM ion concentration. However, a lower concentration is helpful to efficiently investigate the DNA binding sites of the SMC complex.

Third, in the absence of detailed knowledge about the timescales of the ATP hydrolysis, the length of each state during the cyclic transitions was prefixed in the current simulation. In reality, however, these transitions occur stochastically, determined by the rates of ATP binding, ATP hydrolysis, and ADP dissociation, and are likely dependent on the system conformation. Our simulations suggest that careful coordination between the movement of DNA through the SMC and the timing of the transitions between the ATP states is critical at multiple stages of the process. Specifically, we found that if ATP hydrolysis triggers the transition from the engaged to the V-shape state before the DNA segment is captured to form a loop, then DNA translocation cannot occur. Since DNA segment capture was the most time-consuming conformational transition of the overall process in our simulations, the slow ATP hydrolysis rate of the ATPase (58), a common feature of SMC complexes, may precisely serve the purpose of allowing a sufficient time for the formation of a DNA loop within the SMC ring. The experimentally observed DNA-stimulated ATPase activity of SMC (13, 39) may further contribute to coordinating the various steps of the

process by ensuring ATP hydrolysis preferentially occurs when the DNA loop is formed. We also found that excessive residence time in the V-shape state can increase the risk of DNA slippage and failure of translocation (Fig. 5D, left), indicating that a high rate of ADP dissociation may increase the efficiency of the process.

Finally, our simulations considered idealized conditions (SMC translocation on naked DNA) compared to a natural cell environment. Therefore, further investigation is needed to determine whether the translocation process depicted in this study also occurs in cells. Toward this, it is essential to reveal what happens from a molecular point of view when the SMC complexes encounter obstacles on DNA, such as RNA polymerase (72, 73), chromatin proteins (73, 74), transcription factors, and other SMC complexes (31, 75).

MATERIAL AND METHODS

All-atom Molecular Dynamics Simulations

An initial structure of the engaged *Pf*SMC ATPase head dimer was prepared based on the crystal structure (PDB code: 1xex) (39). The E1098Q mutations were modified to wild type. Missing residues and missing C-terminal regions are reconstructed with Modeller 10.1 (43). Water molecules, magnesium ions, and ATP molecules observed in the crystal structure were kept in the simulations. The ATPase domain of the SMC proteins is composed of an N-lobe and a C-lobe region, and the C-terminal of the N-lobe and the N-terminal of the C-lobe are originally connected to the missing coiled-coil arm. To remove effects originating from the terminal charges at these termini, we attached Nme and Ace groups to the C-terminal of the N-lobe and the N-terminal of the C-lobe, respectively.

Since there is no available structure of ATPase-DNA complex for prokaryotic SMCs, we referred to a crystal complex structure of ATPγS-Mre11-Rad50 (a homolog of SMC proteins) and dsDNA complex (PDB code: 5dny) (76). An initial structure of the *Pf*SMC ATPase head-dsDNA complex was modeled following the previous literature (38): (i) The *Pf*SMC ATPase head dimer in the engaged state (PDB code: 1xex) was superimposed onto the ATPase domain in the Rad50-dsDNA complex (PDB code: 5dny). (ii) A target dsDNA was then superimposed onto the dsDNA in the Rad50-dsDNA complex. Here, a 47 bp dsDNA(5'-GGCGA CGTGA TCACC AGATG ATGCT AGATG CTTTC CGAAG AGAGA GC-3') (39) was prepared with x3DNA 2.4

(77, 78). (iii) The superimposed dsDNA was slightly shifted to prevent atomic clashes between the SMC ATPase and dsDNA. Arg and Lys sidechains were set as protonated, while Asp and Glu sidechains were set as deprotonated. Na^+ and Cl^- ions and solvent water molecules were distributed in a rectangular simulation box using AmberTools20 (79). The number of ions was chosen to give an ion concentration of 150 mM.

All MD simulations were performed with OpenMM 7.7.0 (80). The following force fields were adopted: AMBER ff19SB for proteins (81); OL15 for DNA molecules (82); OPC four-point rigid water model (83); Carlson parameters for the ATP molecules (84). We find that choice of all-atom force field does not significantly impact hydrogen bond formation between SMC ATPase heads and DNA (Fig. S11). Coulomb interactions were calculated using the particle mesh Ewald (PME) method (85, 86). The cutoff distance for nonbonded interactions (i.e., Lennard-Jones interaction and direct space term of the PME) was set to 1 nm. Bonds involving hydrogen atoms were constrained using SETTLE (87) for water molecules and SHAKE (88) for proteins, DNA, and ATP molecules. The temperature was controlled at 300 K using a Langevin middle integrator with a friction coefficient of 1.0 ps^{-1} (89), and the pressure was controlled at 1 bar with a Monte Carlo barostat (90, 91). The time step was set to 4.0 fs by adopting a hydrogen-mass repartitioning scheme with a scale factor of 3 for each hydrogen atom (92). Periodic boundary conditions were applied throughout the simulations. Five 1 μs production runs were performed after energy minimization with the L-BFGS algorithm (93) and relaxation simulations with harmonic restraints on the heavy atoms. Configurations were stored every 10 ps. MDTraj (version 1.9.6) (94) was used to post-process trajectory data and analysis.

Definition of Hydrogen Bonds in All-Atom Trajectories

Hydrogen bonds were identified based on Baker-Hubbard criteria (95), where the distance and angle between donor-hydrogen and acceptor satisfy the conditions $r_{\mathrm{H-Acceptor}} < 2.5$ Å and $\theta_{\mathrm{DHA}} > 120$, respectively.

Modelling the full-length SMC-ScpA complex in the disengaged form

We considered the full-length *Py*SMC homodimer model (Fig. S2A), which was previously constructed based on protein cross-linking experiments and crystal

structures of individual domains (20), as a reference structure. We added the ScpA subunit to this model using Modeller 10.1 (43) based on the following additional template structures: (i) the crystal structure of the *Bs*SMC ATPase head domain with the extended coiled-coil bound to NTD of ScpA adopting an extended helix structure (PDB code: 3zgx) (Fig. S2B) (96); (ii) an AlphaFold2-predicted structure (97, 98) of the *Py*SMC ATPase head with the extended coiled-coil bound to the NTD of ScpA adopting a helix-bundle structure (Fig. S2C); (iii) the crystal structure of the *Pf*SMC ATPase head with the extended coiled-coil bound to the CTD of ScpA (PDB code: 5xns) (Fig. S2D) (20).

The ScpA NTD in the first template structure (Fig. S2B) adopts an extended helix conformation and forms a three-helix bundle structure with the coiled-coil of SMC. However, this extended helix is likely a result of crystal packing artifacts induced by domain-swapping and is thermodynamically unfavorable due to exposing hydrophobic residues when the SMC-ScpA complex exists as a monomer (44). On the other hand, cross-link experiments for a prokaryotic *Bs*SMC complex support the four-helix bundle structure in the interface of the ScpA NTD and the SMC coiled-coil (44, 99), consistent with the structure predicted by AlphaFold2 (Fig. S2C). Therefore, the extended part of the ScpA N-terminal helix derived from the first template was excluded in the modeling of the entire SMC-ScpA complex. We regarded a middle region of ScpA as a flexible linker, as it was absent in the template structures. The obtained full-length model of SMC-ScpA in the disengaged form is depicted in Fig. S2E.

Coarse-grained Simulations

We utilized residue-resolution molecular modeling to reproduce the ATP-dependent conformational changes of the SMC-ScpA complex and observe DNA movement coupled with these conformational changes. For the SMC-ScpA complex, we adopted the AICG2+ structure-based model (45), where each amino-acid residue was represented by one bead located on C_α atom position. For DNA, we adopted the 3SPN2.C sequence-dependent model (56), where each nucleotide was represented by three beads located at the positions of base, sugar, and phosphate units. Electrostatic and excluded volume interactions were applied for interactions between the SMC-ScpA complex and DNA unless otherwise stated. The electrostatic interactions were modeled with the Debye-Hückel potential. The charges for globular

parts of the SMC-ScpA were determined by the RESPAC algorithm (100) by distributing them on surface residue beads so that the electrostatic potential around the protein matches the Poisson-Boltzmann estimate based on the all-atom structure. Note that electrostatic interactions by RESPAC charges also include the contributions from salt bridge formation between the SMC ATPase heads and DNA. The standard integer charges (±1 or 0) were used for the flexible linker of ScpA in the middle region. Constant -0.6 charges were placed on the phosphate beads for intra-DNA interactions to consider counter ion condensation, although -1.0 charges were used for protein-DNA interactions.

For the disengaged state, we used the reference structure of the full-length SMC-ScpA model we have built. The intermolecular structure-based interactions between coiled-coil arms were activated only in the final disengaged state of the DNA translocation simulations and in those studying the coiled-coil zipping process in the absence of DNA. In other simulations, these interactions were turned off because the intermolecular hinge interactions and intermolecular ATPase heads interactions are sufficient to maintain the overall I-shape structure (Fig. 2B), and to confirm that changes in the intermolecular interactions between ATPase heads alone can alter the overall structure. For the engaged state, the reference structure of the ATPase heads was based on the crystal structure (PDB code: 1xex, Fig. S2F). The inter-subunit interaction strengths were scaled by a factor of two to accelerate transitions from the disengaged state. The reference structures for the coiled-coil arms and hinge region remain the same as those used in the disengaged state. The hydrogen bond interactions (37) were introduced between the DNA and SMC ATPase heads in the engaged state. These coarse-grained hydrogen-bonding interactions use filter functions in the potential formula so that forces are applied only when the phosphate particles of DNA and the Cα atoms of the protein are within a short range and specific orientation. Note that the coarse-grained hydrogen-bonding interactions are distinguished from long-range electrostatic interactions like salt bridges because the hydrogen bond interactions act only over short distances and with a specific directionality. The coarse-grained hydrogen bonds in our model were set up based on the all-atom simulations. In the residue-resolution model, these hydrogen bonds can be formed by the top 15 amino acid residues (fraction > 0.05) from the all-atom analysis in Fig. 1B. The probability distributions of distance and angles hydrogen-bond parameters (r, θ, φ) were computed for those amino acid residues using one of the

trajectories obtained from the all-atom simulations. The hydrogen-bond parameters were optimized according to the peak positions of the all-atom distributions (Fig. S12). The energy constant ε was set to 4.0 $k_B T$ (~2.4 kcal/mol), within the experimental range for ideal hydrogen bonds. For the V-shape structure, we employed the same reference structure as in the disengaged state but turned off the inter-subunit interactions between the ATPase head domains, as these domains are not expected to stably interact in the V-shape state (44, 53, 54, 101). We adopted the flexible local potential (102) for segments between the hinge and coiled-coil arm in the engaged and V-shape states to enable an open-hinge structure.

Coarse-grained molecular dynamics simulations were performed with CafeMol 3.2.1 (https://www.cafemol.org) (103) by integrating the equations of motion using Langevin dynamics with a step size of 0.2 in the CafeMol time unit. The temperature was set to 300K.

Analysis of DNA Segment Capture and Translocation

The captured DNA loop size was estimated as the difference between the average base positions of DNA in contact with ScpA and those in contact with the coiled-coil arms. We calculated the averages using snapshots from the last 10^7 steps of the engaged state. The translocation step size is estimated as the difference between the average base positions of the DNA in contact with ScpA during the first disengaged state and the average base positions of the DNA segment in contact with ScpA, which was pumped from the SMC ring, in the last disengaged state.

A successful translocation trajectory was defined as one in which the DNA loop is maintained within the SMC ring during the pumping of DNA in the last disengaged state, and where there are discontinuous jumps observed in the DNA base positions contacting with ScpA (Figs. 4IJ and Fig. S7). We defined DNA slippage as a trajectory in which DNA continues to contact with ScpA while sliding around the hinge, coiled-coil, and ATPase head domains, resulting in the gradual destabilization and eventual release of the DNA loop within the SMC ring.

AUTHOR CONTRIBUTIONS

M.Y. and S.T. designed research; M.Y. performed research; M.Y. analyzed data; and M.Y., G.B.B., T.T., and S.T. discussed the data and wrote the paper.

DATA AVAILABILITY

The data that support the findings will be made available upon acceptance.

ACKNOWLEDGEMENT

In this research work, we used the supercomputer of Academic Center for Computing and Media Studies (Kyoto University).

FUNDING

This study was supported by JSPS KAKENHI, Grand Number 20H05934 (S.T.) and 21H02441 (S.T.) and by the MEXT grants JPMXP1020230119 as “Program for Promoting Researches on the Supercomputer Fugaku” (S.T.).

CONFLICT OF INTEREST

The authors declare no conflict of interest.

REFERENCES

1. T. Hirano, At the heart of the chromosome: SMC proteins in action. *Nat. Rev. Mol. Cell Biol.* **7**, 311–322 (2006).
2. E. Kim, R. Barth, C. Dekker, Looping the Genome with SMC Complexes. *Annu. Rev. Biochem.* **92**, 15–41 (2023).
3. T. L. Higashi, F. Uhlmann, SMC complexes: Lifting the lid on loop extrusion. *Curr. Opin. Cell Biol.* **74**, 13–22 (2022).
4. I. F. Davidson, J.-M. Peters, Genome folding through loop extrusion by SMC complexes. *Nat. Rev. Mol. Cell Biol.* **22**, 445–464 (2021).
5. S. Yatskevich, J. Rhodes, K. Nasmyth, Organization of Chromosomal DNA by SMC Complexes. *Annu. Rev. Genet.* **53**, 445–482 (2019).
6. L. Aragón, The Smc5/6 complex: New and old functions of the enigmatic long-distance relative. *Annu. Rev. Genet.* **52**, 89–107 (2018).
7. S. Nolivos, D. Sherratt, The bacterial chromosome: architecture and action of bacterial SMC and SMC-like complexes. *FEMS Microbiol. Rev.* **38**, 380–392 (2014).
8. K. Nasmyth, Disseminating the Genome: Joining, Resolving, and Separating Sister Chromatids During Mitosis and Meiosis. *Annu. Rev. Genet.* **35**, 673–745 (2001).

9. E. Alipour, J. F. Marko, Self-organization of domain structures by DNA-loop-extruding enzymes. *Nucleic Acids Res.* **40**, 11202–11212 (2012).
10. A. Goloborodko, J. F. Marko, L. A. Mirny, Chromosome Compaction by Active Loop Extrusion. *Biophys. J.* **110**, 2162–2168 (2016).
11. A. Goloborodko, M. V. Imakaev, J. F. Marko, L. Mirny, Compaction and segregation of sister chromatids via active loop extrusion. *Elife* **5**, 1–16 (2016).
12. G. Fudenberg, *et al.*, Formation of Chromosomal Domains by Loop Extrusion. *Cell Rep.* **15**, 2038–2049 (2016).
13. T. Terakawa, *et al.*, The condensin complex is a mechanochemical motor that translocates along DNA. *Science (80-.).* **358**, 672–676 (2017).
14. M. Ganji, *et al.*, Real-time imaging of DNA loop extrusion by condensin. *Science (80-.).* **360**, 102–105 (2018).
15. I. F. Davidson, *et al.*, DNA loop extrusion by human cohesin. *Science (80-.).* **366**, 1338–1345 (2019).
16. Y. Kim, Z. Shi, H. Zhang, I. J. Finkelstein, H. Yu, Human cohesin compacts DNA by loop extrusion. *Science (80-.).* **366**, 1345–1349 (2019).
17. B. Pradhan, *et al.*, The Smc5/6 complex is a DNA loop-extruding motor. *Nature* **616**, 843–848 (2023).
18. X. Wang, H. B. Brandão, T. B. K. Le, M. T. Laub, D. Z. Rudner, Bacillus subtilis SMC complexes juxtapose chromosome arms as they travel from origin to terminus. *Science (80-.).* **355**, 524–527 (2017).
19. X. Wang, *et al.*, In Vivo Evidence for ATPase-Dependent DNA Translocation by the Bacillus subtilis SMC Condensin Complex. *Mol. Cell* **71**, 841-847.e5 (2018).
20. M.-L. Diebold-Durand, *et al.*, Structure of Full-Length SMC and Rearrangements Required for Chromosome Organization. *Mol. Cell* **67**, 334-347.e5 (2017).
21. J. F. Marko, P. De Los Rios, A. Barducci, S. Gruber, DNA-segment-capture model for loop extrusion by structural maintenance of chromosome (SMC) protein complexes. *Nucleic Acids Res.* **47**, 6956–6972 (2019).
22. S. K. Nomidis, E. Carlon, S. Gruber, J. F. Marko, DNA tension-modulated translocation and loop extrusion by SMC complexes revealed by molecular dynamics simulations. *Nucleic Acids Res.* **50**, 4974–4987 (2022).

23. M. Kschonsak, *et al.*, Structural Basis for a Safety-Belt Mechanism That Anchors Condensin to Chromosomes. *Cell* **171**, 588-600.e24 (2017).
24. M. Taschner, S. Gruber, DNA segment capture by Smc5/6 holocomplexes. *Nat. Struct. Mol. Biol.* **30**, 619–628 (2023).
25. I. A. Shaltiel, *et al.*, A hold-and-feed mechanism drives directional DNA loop extrusion by condensin. *Science (80-.).* **376**, 1087–1094 (2022).
26. J.-K. Ryu, *et al.*, The condensin holocomplex cycles dynamically between open and collapsed states. *Nat. Struct. Mol. Biol.* **27**, 1134–1141 (2020).
27. J. Ryu, *et al.*, Condensin extrudes DNA loops in steps up to hundreds of base pairs that are generated by ATP binding events. *Nucleic Acids Res.* **50**, 820–832 (2022).
28. B. W. Bauer, *et al.*, Cohesin mediates DNA loop extrusion by a “swing and clamp” mechanism. *Cell* 1–17 (2021). https://doi.org/10.1016/j.cell.2021.09.016.
29. T. L. Higashi, G. Pobegalov, M. Tang, M. I. Molodtsov, F. Uhlmann, A Brownian ratchet model for DNA loop extrusion by the cohesin complex. *Elife* **10**, 1–4 (2021).
30. R. Takaki, A. Dey, G. Shi, D. Thirumalai, Theory and simulations of condensin mediated loop extrusion in DNA. *Nat. Commun.* **12**, 5865 (2021).
31. H. B. Brandão, Z. Ren, X. Karaboja, L. A. Mirny, X. Wang, DNA-loop-extruding SMC complexes can traverse one another in vivo. *Nat. Struct. Mol. Biol.* **28**, 642–651 (2021).
32. B. Lee, J. Rhodes, J. Löwe, Clamping of DNA shuts the condensin neck gate. *Proc. Natl. Acad. Sci.* **119**, 1–10 (2022).
33. Z. Shi, H. Gao, X. Bai, H. Yu, Cryo-EM structure of the human cohesin-NIPBL-DNA complex. *Science (80-.).* **368**, 1454–1459 (2020).
34. J. E. Collier, *et al.*, Transport of DNA within cohesin involves clamping on top of engaged heads by Scc2 and entrapment within the ring by Scc3. *Elife* **9**, 1–36 (2020).
35. Y. Yu, *et al.*, Cryo-EM structure of DNA-bound Smc5/6 reveals DNA clamping enabled by multi-subunit conformational changes. *Proc. Natl. Acad. Sci.* **119**, 1–10 (2022).

36. F. Bürmann, L. F. H. H. Funke, J. W. Chin, J. Löwe, Cryo-EM structure of MukBEF reveals DNA loop entrapment at chromosomal unloading sites. *Mol. Cell* 1–16 (2021). https://doi.org/10.1016/j.molcel.2021.10.011.
37. T. Niina, G. B. Brandani, C. Tan, S. Takada, Sequence-dependent nucleosome sliding in rotation-coupled and uncoupled modes revealed by molecular simulations. *PLOS Comput. Biol.* **13**, e1005880 (2017).
38. R. Vazquez Nunez, L. B. Ruiz Avila, S. Gruber, Transient DNA Occupancy of the SMC Interarm Space in Prokaryotic Condensin. *Mol. Cell* **75**, 209-223.e6 (2019).
39. A. Lammens, A. Schele, K.-P. Hopfner, Structural Biochemistry of ATP-Driven Dimerization and DNA-Stimulated Activation of SMC ATPases. *Curr. Biol.* **14**, 1778–1782 (2004).
40. D. Krepel, R. R. Cheng, M. Di Pierro, J. N. Onuchic, Deciphering the structure of the condensin protein complex. *Proc. Natl. Acad. Sci.* **115**, 11911–11916 (2018).
41. D. Krepel, A. Davtyan, N. P. Schafer, P. G. Wolynes, J. N. Onuchic, Braiding topology and the energy landscape of chromosome organization proteins. *Proc. Natl. Acad. Sci.* **117**, 1468–1477 (2020).
42. J.-H. Jeon, *et al.*, Evidence for binary Smc complexes lacking kite subunits in archaea. *IUCrJ* **7**, 193–206 (2020).
43. B. Webb, A. Sali, Comparative Protein Structure Modeling Using MODELLER. *Curr. Protoc. Bioinforma.* **54** (2016).
44. K. Kamada, M. Su'etsugu, H. Takada, M. Miyata, T. Hirano, Overall Shapes of the SMC-ScpAB Complex Are Determined by Balance between Constraint and Relaxation of Its Structural Parts. *Structure* **25**, 603-616.e4 (2017).
45. W. Li, W. Wang, S. Takada, Energy landscape views for interplays among folding, binding, and allostery of calmodulin domains. *Proc. Natl. Acad. Sci.* **111**, 10550–10555 (2014).
46. G. B. Brandani, T. Niina, C. Tan, S. Takada, DNA sliding in nucleosomes via twist defect propagation revealed by molecular simulations. *Nucleic Acids Res.* **46**, 2788–2801 (2018).
47. C. Tan, S. Takada, Nucleosome allostery in pioneer transcription factor binding. *Proc. Natl. Acad. Sci. U. S. A.* **117**, 20586–20596 (2020).

48. F. Nagae, G. B. Brandani, S. Takada, T. Terakawa, The lane-switch mechanism for nucleosome repositioning by DNA translocase. *Nucleic Acids Res.* **49**, 9066–9076 (2021).
49. F. Nagae, S. Takada, T. Terakawa, Histone chaperone Nap1 dismantles an H2A/H2B dimer from a partially unwrapped nucleosome. *Nucleic Acids Res.* **51**, 5351–5363 (2023).
50. G. B. Brandani, S. Gopi, M. Yamauchi, S. Takada, Molecular dynamics simulations for the study of chromatin biology. *Curr. Opin. Struct. Biol.* **77**, 102485 (2022).
51. N. Koga, S. Takada, Folding-based molecular simulations reveal mechanisms of the rotary motor F1-ATPase. *Proc. Natl. Acad. Sci.* **103**, 5367–5372 (2006).
52. M. Hirano, D. E. Anderson, H. P. Erickson, T. Hirano, Bimodal activation of SMC ATPase by intra- and inter-molecular interactions. *EMBO J.* **20**, 3238–3250 (2001).
53. M. Hirano, T. Hirano, Opening Closed Arms: Long-Distance Activation of SMC ATPase by Hinge-DNA Interactions. *Mol. Cell* **21**, 175–186 (2006).
54. T. E. Melby, C. N. Ciampaglio, G. Briscoe, H. P. Erickson, The Symmetrical Structure of Structural Maintenance of Chromosomes (SMC) and MukB Proteins: Long, Antiparallel Coiled Coils, Folded at a Flexible Hinge. *J. Cell Biol.* **142**, 1595–1604 (1998).
55. H. Koide, N. Kodera, S. Bisht, S. Takada, T. Terakawa, Modeling of DNA binding to the condensin hinge domain using molecular dynamics simulations guided by atomic force microscopy. *PLoS Comput. Biol.* **17**, e1009265 (2021).
56. G. S. Freeman, D. M. Hinckley, J. P. Lequieu, J. K. Whitmer, J. J. de Pablo, Coarse-grained modeling of DNA curvature. *J. Chem. Phys.* **141**, 165103 (2014).
57. J. J. Griese, K.-P. Hopfner, Structure and DNA-binding activity of the Pyrococcus furiosus SMC protein hinge domain. *Proteins Struct. Funct. Bioinforma.* **79**, 558–568 (2011).
58. M. Hassler, I. A. Shaltiel, C. H. Haering, Towards a Unified Model of SMC Complex Function. *Curr. Biol.* **28**, R1266–R1281 (2018).
59. F. Bürmann, *et al.*, Tuned SMC Arms Drive Chromosomal Loading of Prokaryotic Condensin. *Mol. Cell* **65**, 861-872.e9 (2017).

60. N. T. Tran, M. T. Laub, T. B. K. Le, SMC Progressively Aligns Chromosomal Arms in Caulobacter crescentus but Is Antagonized by Convergent Transcription. *Cell Rep.* **20**, 2057–2071 (2017).
61. R. Janissen, *et al.*, All eukaryotic SMC proteins induce a twist of -0.6 at each DNA-loop-extrusion step. *bioRxiv* **5** (2024).
62. B. G. Lee, *et al.*, Cryo-EM structures of holo condensin reveal a subunit flip-flop mechanism. *Nat. Struct. Mol. Biol.* **27**, 743–751 (2020).
63. F. Bürmann, *et al.*, A folded conformation of MukBEF and cohesin. *Nat. Struct. Mol. Biol.* **26**, 227–236 (2019).
64. N. J. Petela, *et al.*, Folding of cohesin's coiled coil is important for Scc2/4-induced association with chromosomes. *Elife* **10**, 1–32 (2021).
65. S. T. Hallett, *et al.*, Cryo-EM structure of the Smc5/6 holo-complex. *Nucleic Acids Res.* **50**, 9505–9520 (2022).
66. Y. Yu, *et al.*, Integrative analysis reveals unique structural and functional features of the Smc5/6 complex. *Proc. Natl. Acad. Sci.* **118**, e2026844118 (2021).
67. J.-H. Prinz, *et al.*, Markov models of molecular kinetics: Generation and validation. *J. Chem. Phys.* **134**, 174105 (2011).
68. B. E. Husic, V. S. Pande, Markov State Models: From an Art to a Science. *J. Am. Chem. Soc.* **140**, 2386–2396 (2018).
69. J. Hénin, T. Lelièvre, M. R. Shirts, O. Valsson, L. Delemotte, Enhanced Sampling Methods for Molecular Dynamics Simulations [Article v1.0]. *Living J. Comput. Mol. Sci.* **4**, 1–60 (2022).
70. K. -i. Okazaki, N. Koga, S. Takada, J. N. Onuchic, P. G. Wolynes, Multiple-basin energy landscapes for large-amplitude conformational motions of proteins: Structure-based molecular dynamics simulations. *Proc. Natl. Acad. Sci.* **103**, 11844–11849 (2006).
71. J.-L. Birrien, *et al.*, Pyrococcus yayanosii sp. nov., an obligate piezophilic hyperthermophilic archaeon isolated from a deep-sea hydrothermal vent. *Int. J. Syst. Evol. Microbiol.* **61**, 2827–2881 (2011).
72. H. B. Brandão, *et al.*, RNA polymerases as moving barriers to condensin loop extrusion. *Proc. Natl. Acad. Sci. U. S. A.* **116**, 20489–20499 (2019).

73. B. Pradhan, *et al.*, SMC Complexes Can Traverse Physical Roadblocks Bigger Than Their Ring Size. *SSRN Electron. J.* 1–17 (2022). https://doi.org/10.2139/ssrn.4046136.
74. K. Yamaura, *et al.*, Chromosomal domain formation by archaeal SMC, a roadblock protein, and DNA structure. *bioRxiv* 2024.05.14.594075 (2024).
75. E. Kim, J. Kerssemakers, I. A. Shaltiel, C. H. Haering, C. Dekker, DNA-loop extruding condensin complexes can traverse one another. *Nature* **579**, 438–442 (2020).
76. Y. Liu, *et al.*, <scp>ATP</scp> -dependent <scp>DNA</scp> binding, unwinding, and resection by the Mre11/Rad50 complex. *EMBO J.* **35**, 743–758 (2016).
77. X.-J. Lu, 3DNA: a software package for the analysis, rebuilding and visualization of three-dimensional nucleic acid structures. *Nucleic Acids Res.* **31**, 5108–5121 (2003).
78. X.-J. Lu, W. K. Olson, 3DNA: a versatile, integrated software system for the analysis, rebuilding and visualization of three-dimensional nucleic-acid structures. *Nat. Protoc.* **3**, 1213–1227 (2008).
79. D. M. Y. and P. A. K. D.A. Case, K. Belfon, I.Y. Ben-Shalom, S.R. Brozell, D.S. Cerutti, T.E. Cheatham, III, V.W.D. Cruzeiro, T.A. Darden, R.E. Duke, G. Giambasu, M.K. Gilson, H. Gohlke, A.W. Goetz, R Harris, S. Izadi, S.A. Izmailov, K. Kasavajhala, A. Kovalenko, R. Krasny, T., AMBER 2020. (2020). Available at: https://ambermd.org/index.php.
80. P. Eastman, *et al.*, OpenMM 7: Rapid development of high performance algorithms for molecular dynamics. *PLOS Comput. Biol.* **13**, e1005659 (2017).
81. C. Tian, *et al.*, ff19SB: Amino-Acid-Specific Protein Backbone Parameters Trained against Quantum Mechanics Energy Surfaces in Solution. *J. Chem. Theory Comput.* **16**, 528–552 (2020).
82. M. Zgarbová, *et al.*, Refinement of the Sugar-Phosphate Backbone Torsion Beta for AMBER Force Fields Improves the Description of Z- and B-DNA. *J. Chem. Theory Comput.* **11**, 5723–5736 (2015).
83. S. Izadi, R. Anandakrishnan, A. V Onufriev, Building Water Models: A Different Approach. *J. Phys. Chem. Lett.* **5**, 3863–3871 (2014).

84. K. L. Meagher, L. T. Redman, H. A. Carlson, Development of polyphosphate parameters for use with the AMBER force field. *J. Comput. Chem.* **24**, 1016–1025 (2003).
85. T. Darden, D. York, L. Pedersen, Particle mesh Ewald: An N log(N) method for Ewald sums in large systems. *J. Chem. Phys.* **98**, 10089–10092 (1993).
86. U. Essmann, *et al.*, A smooth particle mesh Ewald method. *J. Chem. Phys.* **103**, 8577–8593 (1995).
87. S. Miyamoto, P. A. Kollman, Settle: An analytical version of the SHAKE and RATTLE algorithm for rigid water models. *J. Comput. Chem.* **13**, 952–962 (1992).
88. J.-P. Ryckaert, G. Ciccotti, H. J. C. Berendsen, Numerical integration of the cartesian equations of motion of a system with constraints: molecular dynamics of n-alkanes. *J. Comput. Phys.* **23**, 327–341 (1977).
89. Z. Zhang, X. Liu, K. Yan, M. E. Tuckerman, J. Liu, Unified Efficient Thermostat Scheme for the Canonical Ensemble with Holonomic or Isokinetic Constraints via Molecular Dynamics. *J. Phys. Chem. A* **123**, 6056–6079 (2019).
90. K. H. Chow, D. M. Ferguson, Isothermal-isobaric molecular dynamics simulations with Monte Carlo volume sampling. *Comput. Phys. Commun.* **91**, 283–289 (1995).
91. J. Åqvist, P. Wennerström, M. Nervall, S. Bjelic, B. O. Brandsdal, Molecular dynamics simulations of water and biomolecules with a Monte Carlo constant pressure algorithm. *Chem. Phys. Lett.* **384**, 288–294 (2004).
92. C. W. Hopkins, S. Le Grand, R. C. Walker, A. E. Roitberg, Long-Time-Step Molecular Dynamics through Hydrogen Mass Repartitioning. *J. Chem. Theory Comput.* **11**, 1864–1874 (2015).
93. D. C. Liu, J. Nocedal, On the limited memory BFGS method for large scale optimization. *Math. Program.* **45**, 503–528 (1989).
94. R. T. McGibbon, *et al.*, MDTraj: A Modern Open Library for the Analysis of Molecular Dynamics Trajectories. *Biophys. J.* **109**, 1528–1532 (2015).
95. E. N. Baker, R. E. Hubbard, Hydrogen bonding in globular proteins. *Prog. Biophys. Mol. Biol.* **44**, 97–179 (1984).
96. F. Bürmann, *et al.*, An asymmetric SMC–kleisin bridge in prokaryotic condensin. *Nat. Struct. Mol. Biol.* **20**, 371–379 (2013).

97. J. Jumper, *et al.*, Highly accurate protein structure prediction with AlphaFold. *Nature* (2021). https://doi.org/10.1038/s41586-021-03819-2.
98. M. Mirdita, *et al.*, ColabFold: making protein folding accessible to all. *Nat. Methods* **19**, 679–682 (2022).
99. T. G. Gligoris, *et al.*, Closing the cohesin ring: Structure and function of its Smc3-kleisin interface. *Science (80-.).* **346**, 963–967 (2014).
100. T. Terakawa, S. Takada, RESPAC: Method to Determine Partial Charges in Coarse-Grained Protein Model and Its Application to DNA-Binding Proteins. *J. Chem. Theory Comput.* **10**, 711–721 (2014).
101. M. Hirano, Bimodal activation of SMC ATPase by intra- and inter-molecular interactions. *EMBO J.* **20**, 3238–3250 (2001).
102. T. Terakawa, S. Takada, Multiscale ensemble modeling of intrinsically disordered proteins: P53 N-terminal domain. *Biophys. J.* **101**, 1450–1458 (2011).
103. H. Kenzaki, *et al.*, CafeMol: A Coarse-Grained Biomolecular Simulator for Simulating Proteins at Work. *J. Chem. Theory Comput.* **7**, 1979–1989 (2011).

FIGURES

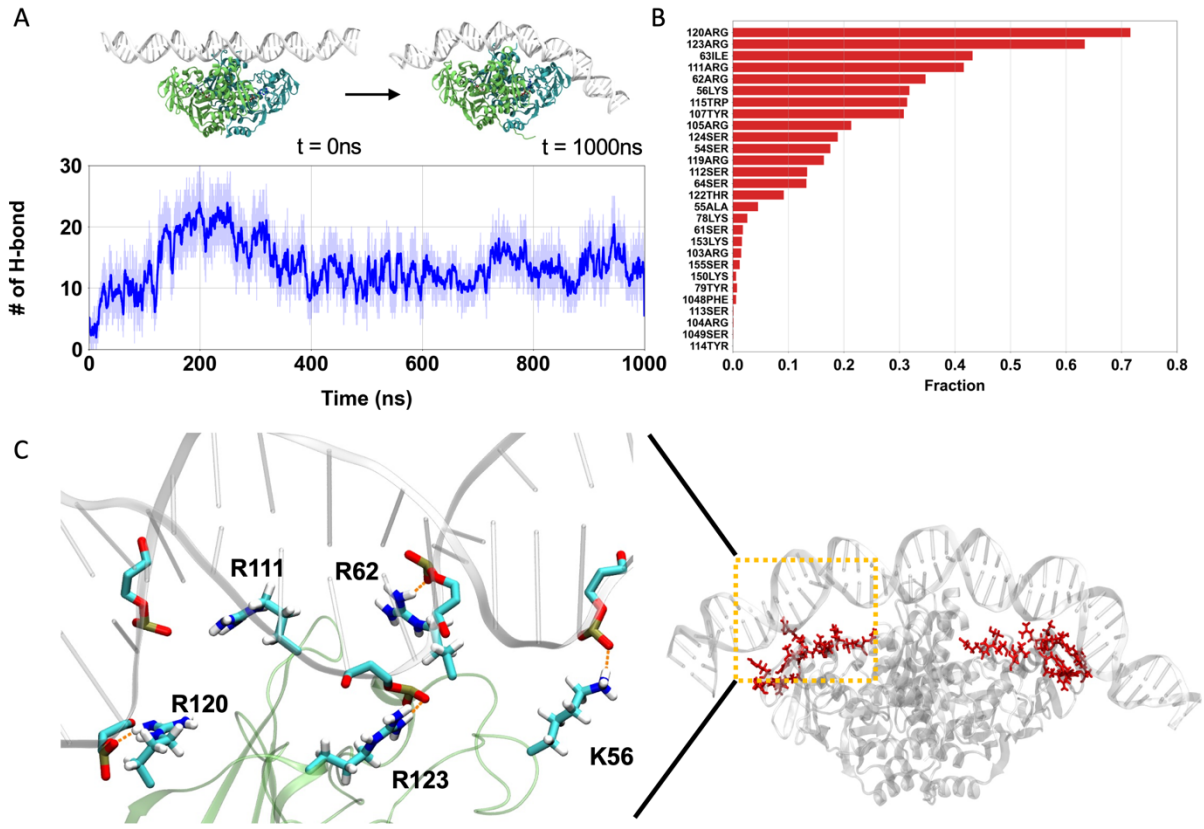

Figure 1: All-atom MD simulations of engaged *Pf*SMC ATPase heads and DNA. (A) A representative trajectory of all-atom MD. (Upper) Left and right depict the initial and final snapshots, respectively. (Lower) Time series of the number of hydrogen bonds between ATPase heads and DNA. (B) The fraction of hydrogen formation between amino acid residues in the ATPase heads and DNA. (C) A representative snapshot of the hydrogen-bond forming residues. (Left) Hydrogen bond network between the ATPase heads and DNA for representative basic residues. (Right) The hydrogen bond forming residues are positioned on the top surface of ATPase heads.

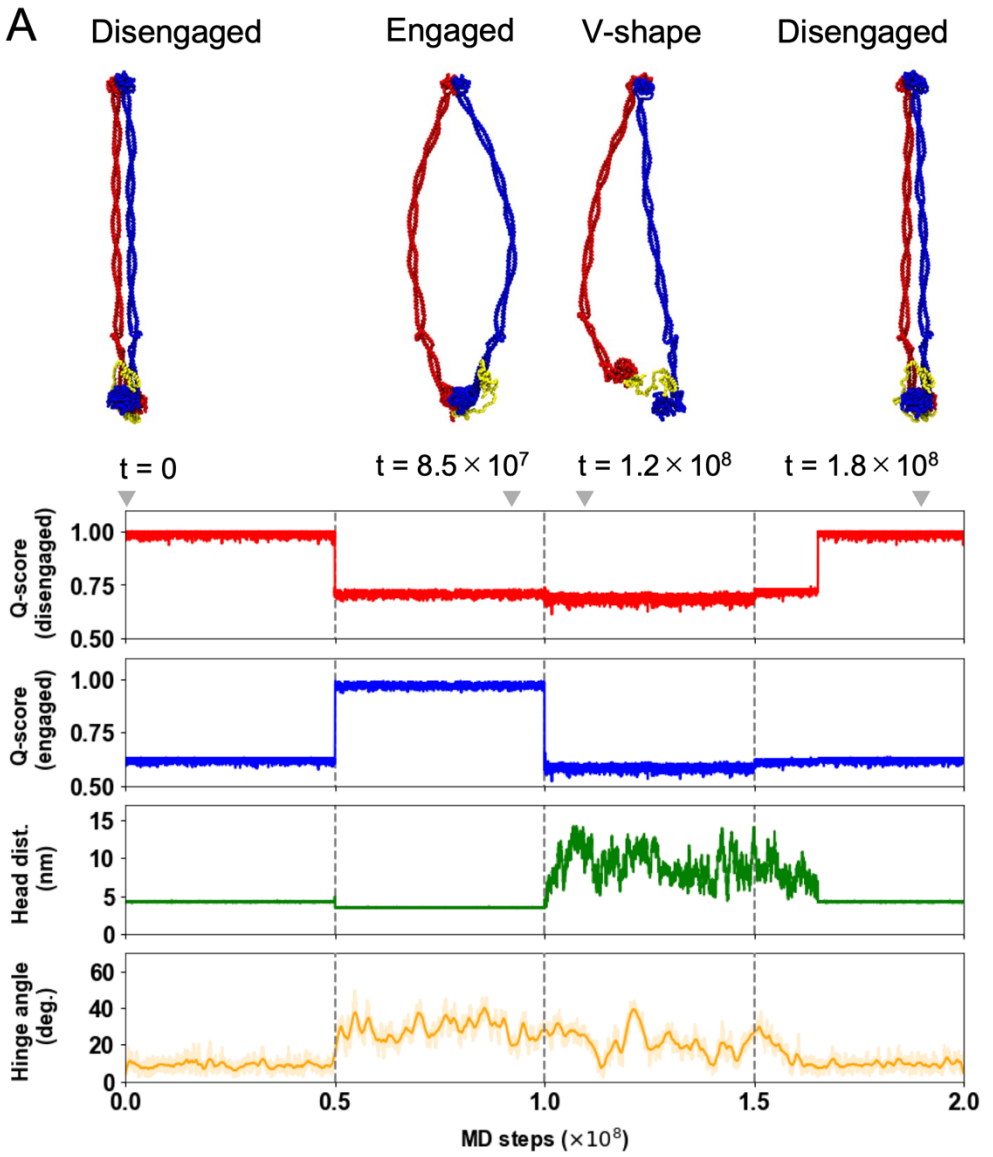
A
Disengaged
Engaged
V-shape
Disengaged
t = 0
t = 8.5 × 10^7
t = 1.2 × 10^8
t = 1.8 × 10^8
Q-score (disengaged)
Q-score (engaged)
Head dist. (nm)
Hinge angle (deg.)
MD steps (×10^8)

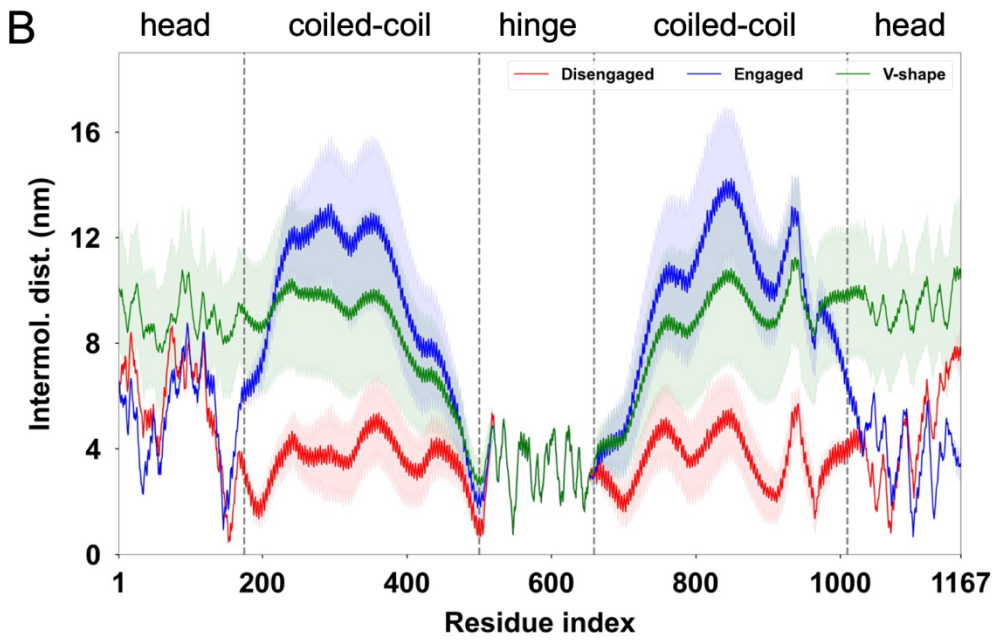
B
head
coiled-coil
hinge
coiled-coil
head
Disengaged
Engaged
V-shape
Intermol. dist. (nm)
Residue index

Figure 2: MD simulations for ATP-dependent conformational changes of SMC-ScpA complex. (A) A representative trajectory of ATP-dependent conformational changes in the SMC complex by switching the reference structures in the AICG2+ model. (Top) Typical snapshots of SMC-ScpA complex for the disengaged (t = 0 step), engaged (t = 8.5×10^7 steps), V-shape (t = 1.2×10^8 steps), and disengaged (t = 1.8×10^8 steps) states. (Bottom) Times series of Q-scores for the disengaged and engaged structure, head-head distance, and hinge angle. The head-head distance is defined as the center of distance between two ATPase head domains. The hinge angle is calculated for three selected points; The center of mass of the hinge dimerization domain defines one point. The other two points are defined by the center of mass of the sequential 10 amino acid residues in the coiled-coil middle region for each chain. (B) Average distances between intermolecular amino acid residues with the same index number for the disengaged (red), engaged(blue), and V-shape (green) structures.

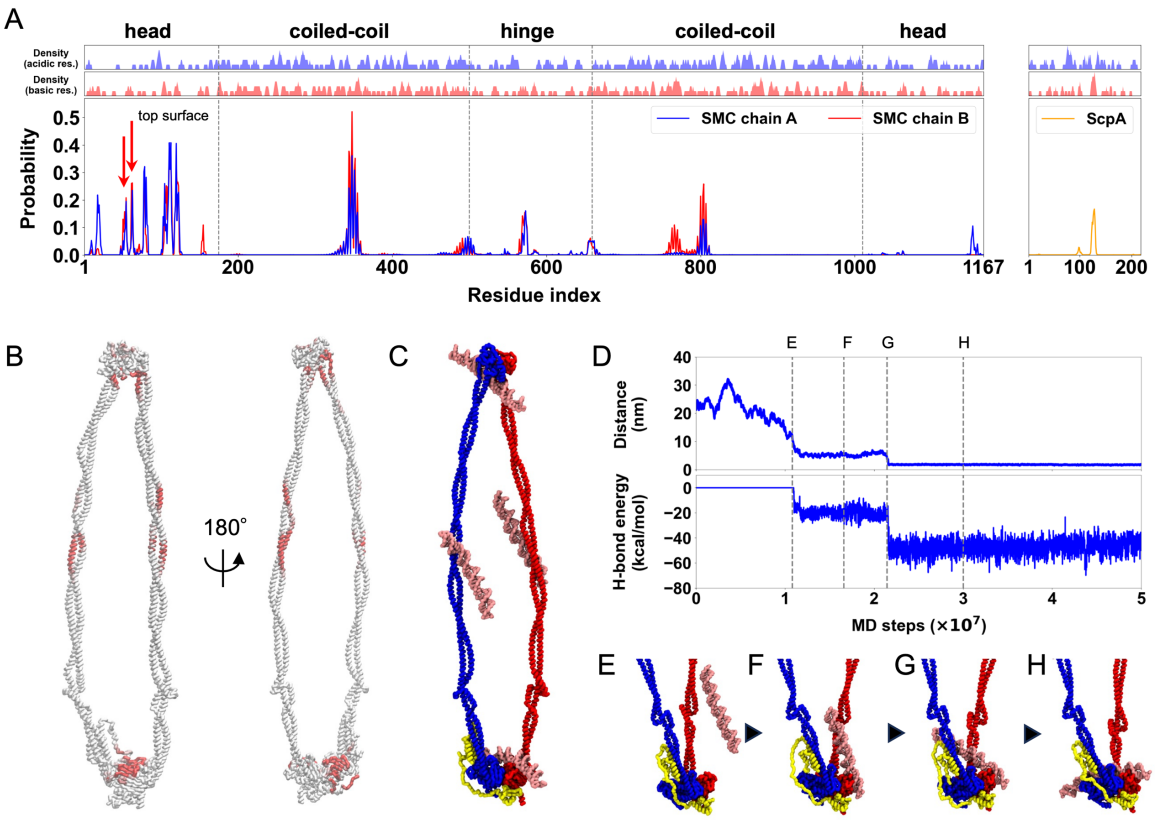

Figure 3: Identification of DNA binding sites in the SMC-ScpA complex. (A) Top two panels plot the local average of charges defined as the moving average with a window size of 5 residues. Bottom panel plots the contact probability between DNA and SMC-ScpA complex. (B) DNA contact probability mapped on the SMC-ScpA structure. (C) A typical snapshot of DNA binding to the SMC-ScpA complex. (D) Upper panel plots timeseries of the distance between center of mass of the ATPase heads and DNA. Lower panel plots timeseries of the hydrogen-bond energy. (E-H) Representative snapshots during a DNA binding event to the top of the SMC ATPase heads.

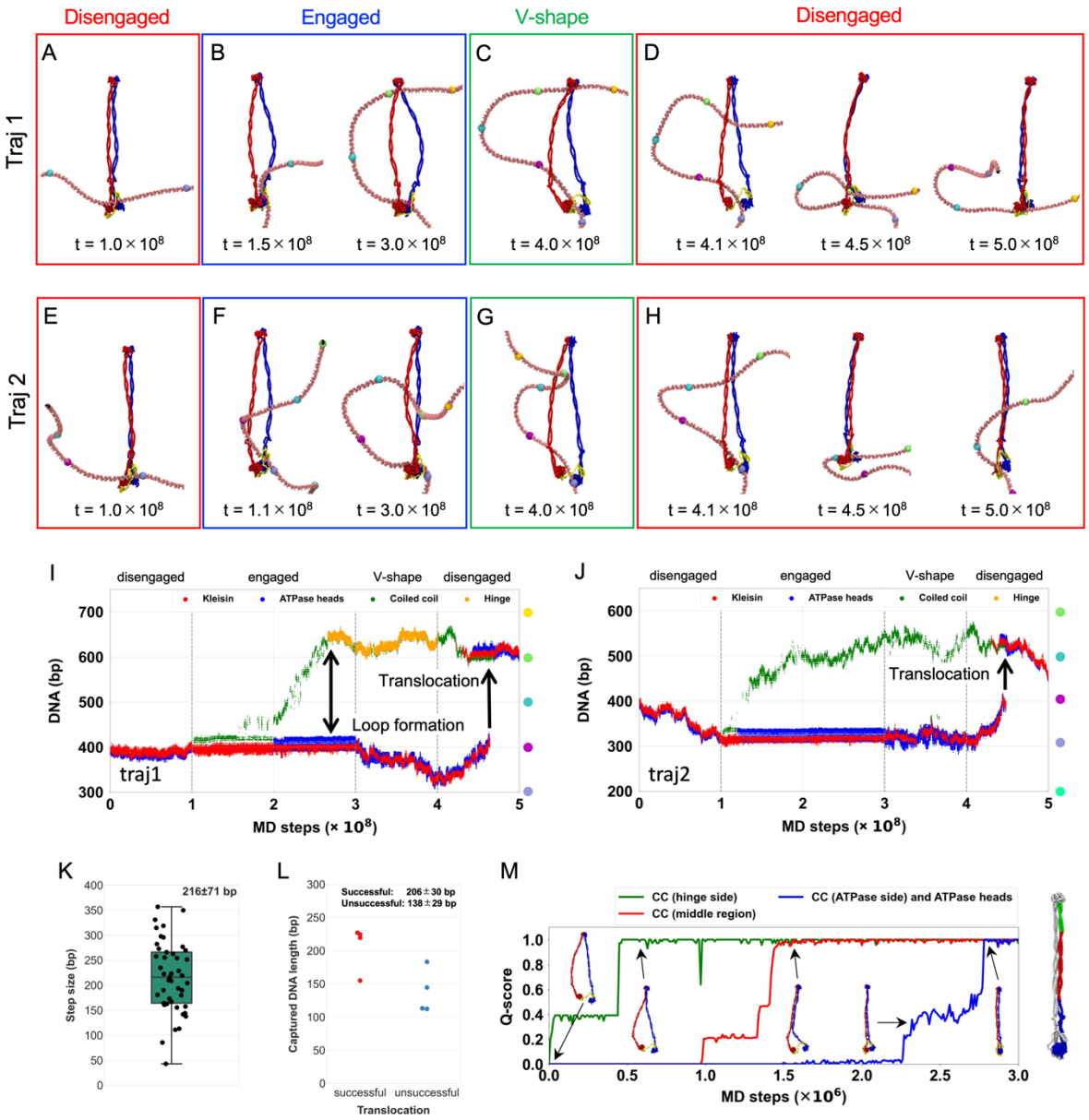

Figure 4: SMC translocation along DNA via DNA-segment capture. (A-D) A representative trajectory of DNA translocation by the SMC-ScpA complex coupled with the conformational change depending on the nucleotide states. The DNA reaches the hinge domain in the engaged state. (E-H) A representative trajectory of DNA translocation by the SMC-ScpA complex coupled with the conformational change depending on the nucleotide states. The DNA does not reach the hinge in the engaged state. (I-J) Time series of the DNA position where each SMC domain contacts with. DNA-Protein contacts at kleisin, ATPase heads, coiled-coil, and hinge domains are plotted in red, blue, green, and orange, respectively. (K) Analysis of translocation step size. (L) The length of the captured DNA segment in the engaged state for successful (left) and unsuccessful (right) translocation trajectories. (M) Q-scores, i.e., the fraction

of native contacts, between the intermolecular coiled-coil arm and ATPase head domains, revealing the zipping motion of the coiled-coil arm when transitioning from the V-shape to the disengaged state. The coiled-coil arm was divided into three domains: hinge side (green), middle region (red), and ATPase heads side (blue).

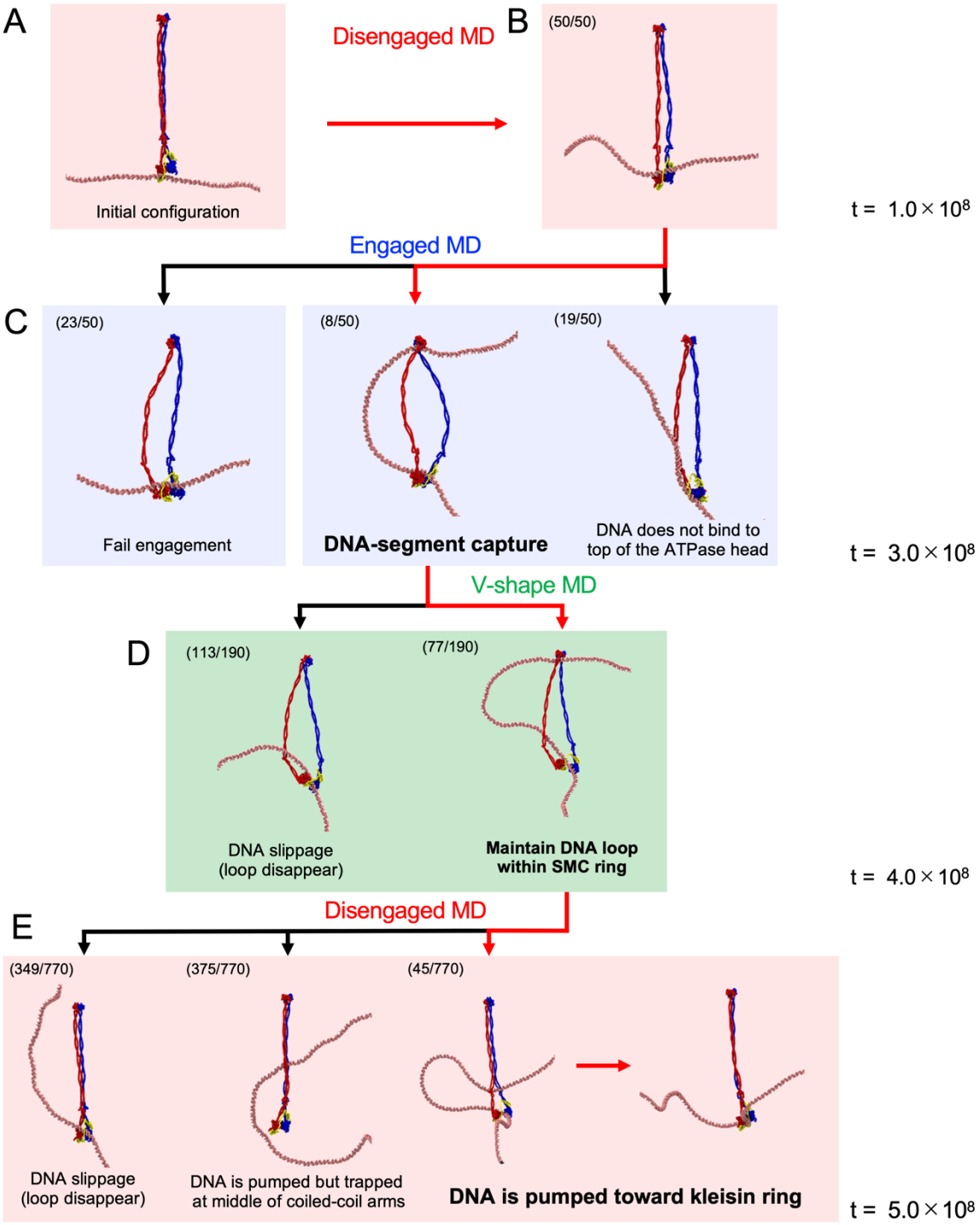

Figure 5: Diverse DNA dynamics during ATP hydrolysis cycle. The numbers at the top left represent the number of trajectories observed. (A) Initial configuration of the simulations. (B) The results of disengaged MD simulations. (C) The results of engaged MD simulations. Each simulation was restarted from the final snapshot of each disengaged MD simulation. (D) The results of V-shape MD simulations. Multiple simulations were conducted by restarting from the DNA-segment capture trajectories

in the engaged state€) The results of disengaged MD simulations. The simulations were restarted from the V-shape conformations maintaining the DNA loop within the SMC ring.

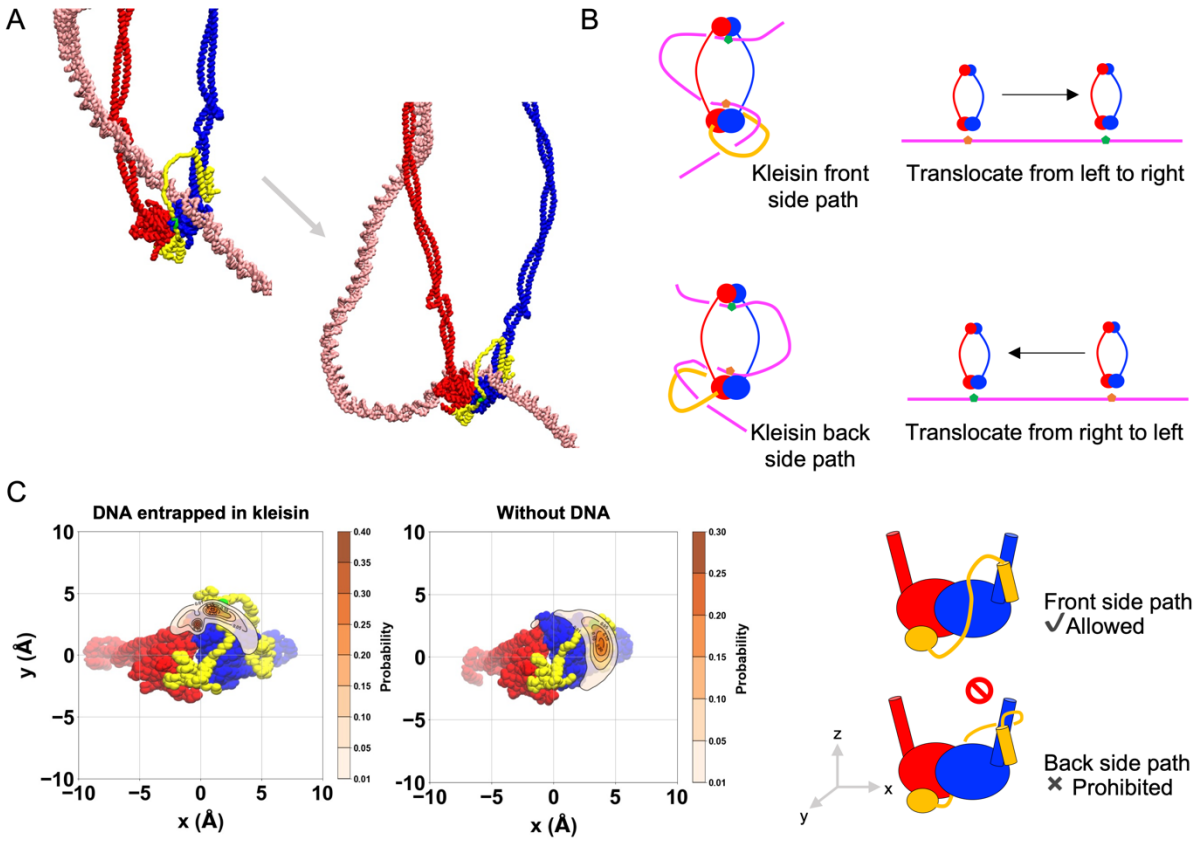

Figure 6: Asymmetric kleisin path makes unidirectionality of SMC translocation. (A) Typical snapshots of the moment when the SMC-ScpA complex captured a DNA segment within its ring structure in the engaged state. Particles marked in green on the ScpA indicate DNA patches. (B) Schematic figures highliting how the kleisin path determined the direction of translocation. (C) The spatial distribution of the DNA patch on the ScpA subunit.

Movie S1: The representative trajectory of all-atom MD simulations for engaged *Pf*SMC ATPase heads and DNA.

Movie S2: The representative trajectory of ATP-dependent conformational changes of SMC-ScpA complex.

Movie S3: The representative trajectory of DNA binding events to the top of ATPase heads.

Movie S4: The representative trajectory of SMC-ScpA translocation along DNA, in which the DNA reaches the hinge domain in the engaged state.

Movie S5: The representative trajectory of SMC-ScpA translocation along DNA, in which the DNA does not reach the hinge domain in the engaged state.

Movie S6: The representative trajectory of zipping up the coiled-coil arm when transition from V-shape to disengaged states.

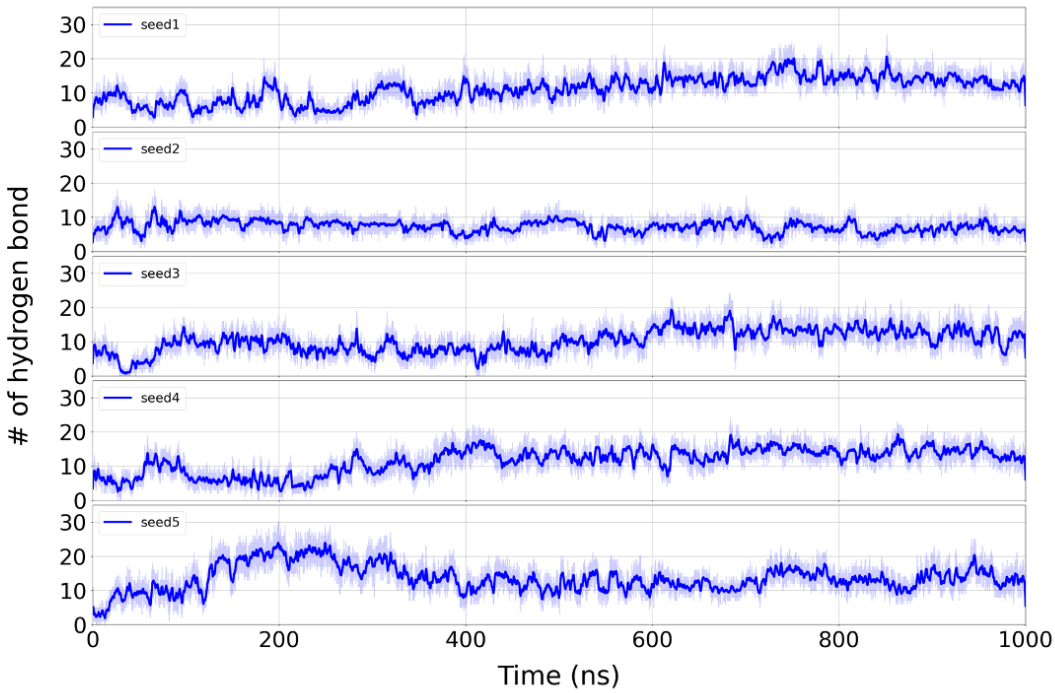

Supplementary Figure S1: Time series of the number of hydrogen bonds between *Pf*SMC ATPase and DNA derived from all-atom MD simulations.

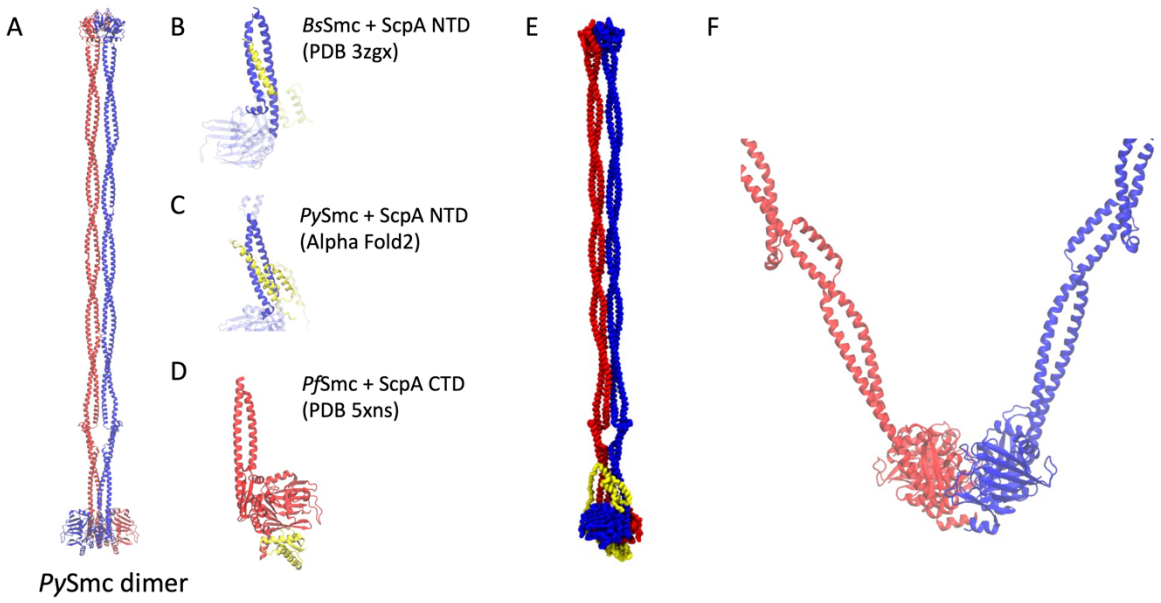

Supplementary Figure S2: Modeling of a full-length *Py*SMC-ScpA complex. (A-D) Template structures for homology modeling of a full-length *Py*SMC-ScpA complex. The regions ignored in the homology modeling are indicated by transpare€ (E) A coarse-grained full-length *Py*SMC-ScpA complex model where one amino acid is represented by one bead. (F) A homology model of the engaged ATPase heads based on a crystal structure (PDB code: 1xex). The coiled-coil arms connected to the ATPase heads are modelled based on the I-shaped SMC dimer model in panel A.

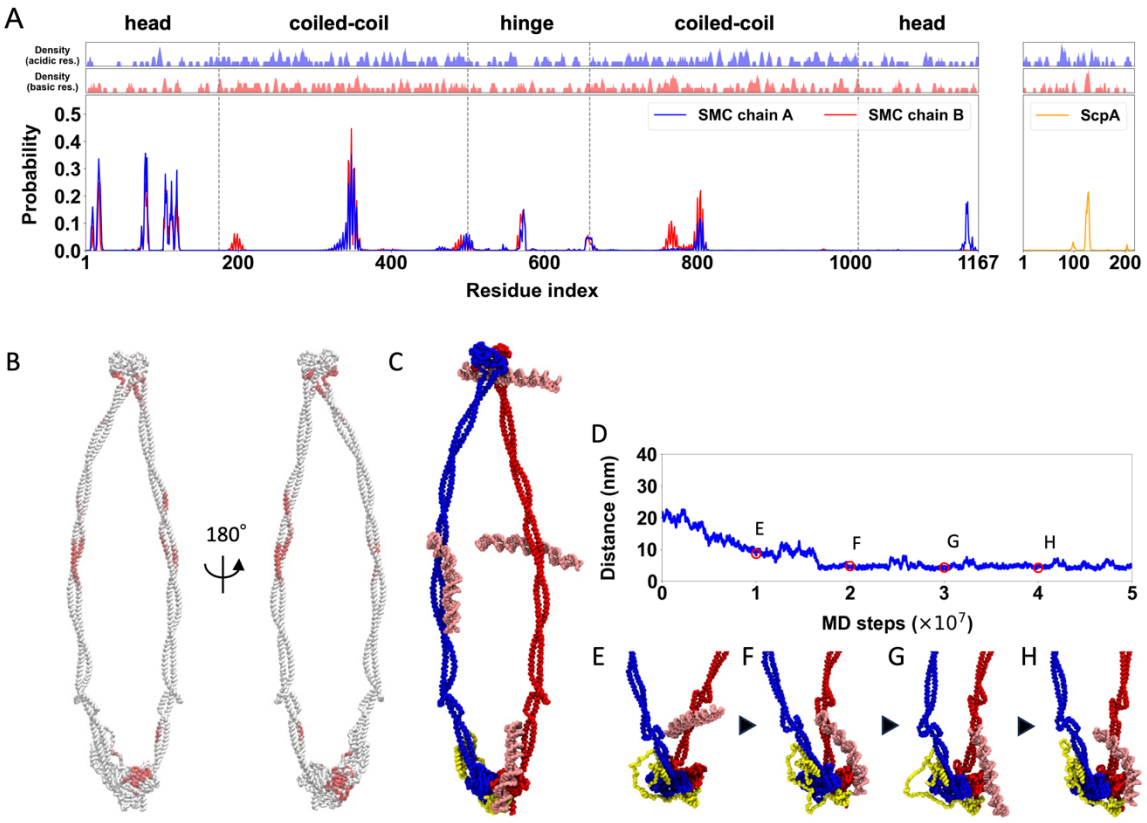

Supplementary Figure S3: DNA binding sites in the SMC-ScpA complex where hydrogen bond interactions on the ATPase heads are not incorporated. (A) Top two panels plot the local average of charges defined as the moving average with window size of 5 residues. Bottom panel plots the contact probability between DNA and SMC-ScpA complex. (B) DNA contact probability mapped on the SMC-ScpA structure. (C) A typical snapshot of DNA binding to the SMC-ScpA complex. The DNA that binds to the ATPase heads does not migrate to the top, staying on the side surface of the ATPase heads. (D) A representative timeseries of the distance between center of mass of the ATPase heads and DNA. (E-H) Representative snapshots during a DNA binding event to the SMC ATPase heads.

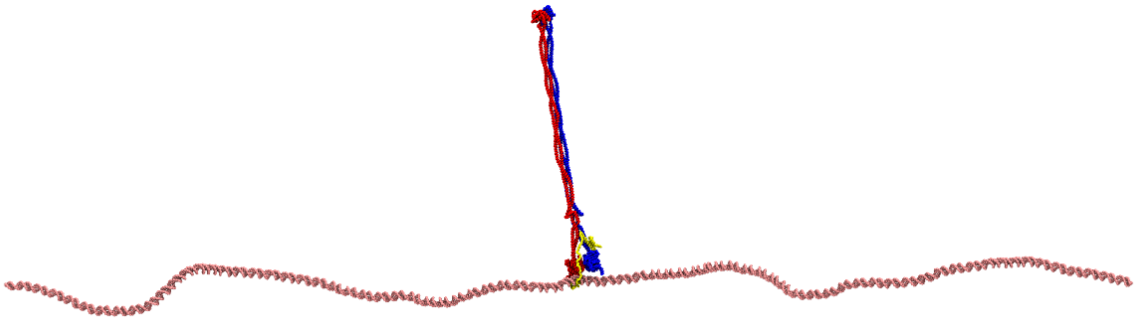

Supplemental Figure S4: An initial structure of DNA translocation simulations. An 800 bp dsDNA was placed into the kleisin ring of the disengaged state of the SMC-ScpA complex.

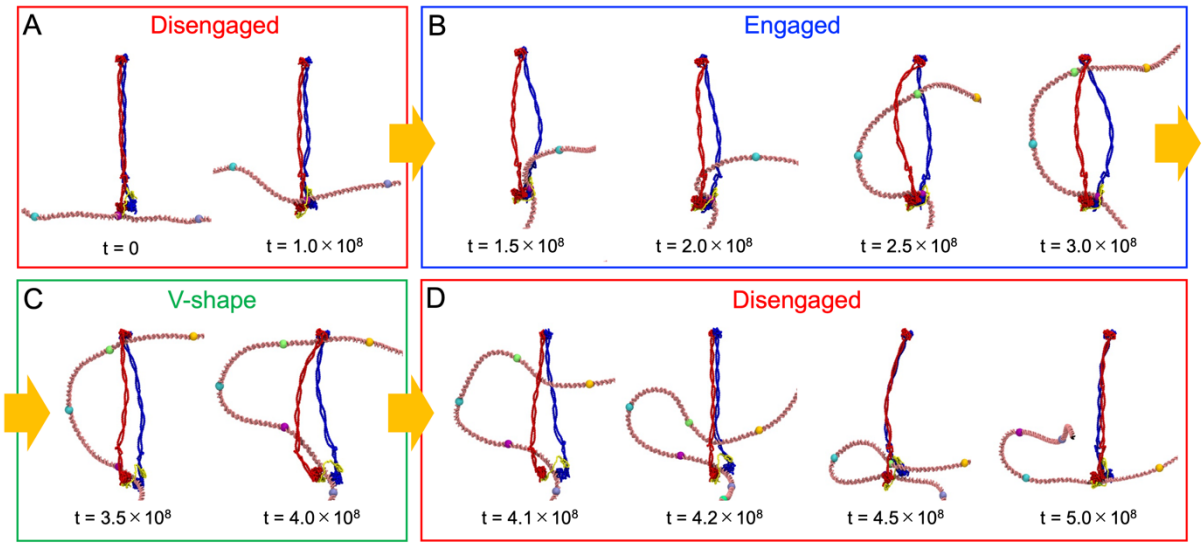

Supplementary Figure S5: Detail snapshots during DNA translocation via DNA-segment capture. (A) The disengaged state during t = 0 - 1.0×10^8 MD steps. (B) The engaged state during t = 1.0×10^8 - 3.0×10^8 MD steps. (C) The V-shape state during t = 3.0×10^8 - 4.0×10^8 MD steps. (D) The disengaged state t = 4.0×10^8 – 5.0×10^8 MD steps.

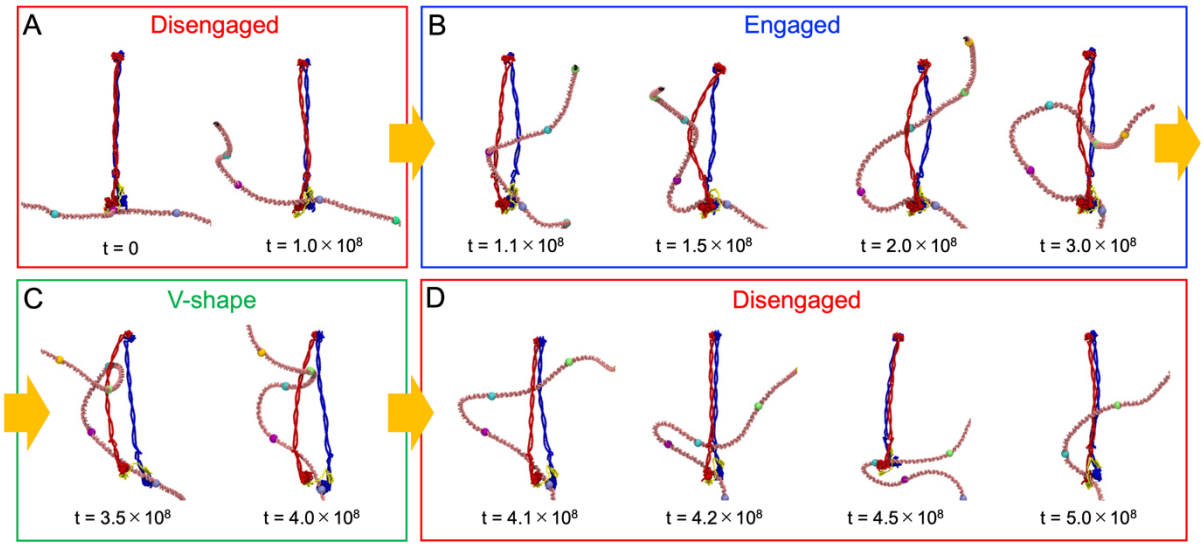

Supplementary Figure S6: Detail snapshots during DNA translocation via DNA-segment capture where the DNA does not reach the hinge domain in the engaged state. (A) The disengaged state during t = 0 - 1.0×10^8 MD steps. (B) The engaged state during t = 1.0×10^8 - 3.0×10^8 MD steps. (C) The V-shape state during t = 3.0×10^8 - 4.0×10^8 MD steps. (D) The disengaged state during t = 4.0×10^8 - 5.0×10^8 MD steps.

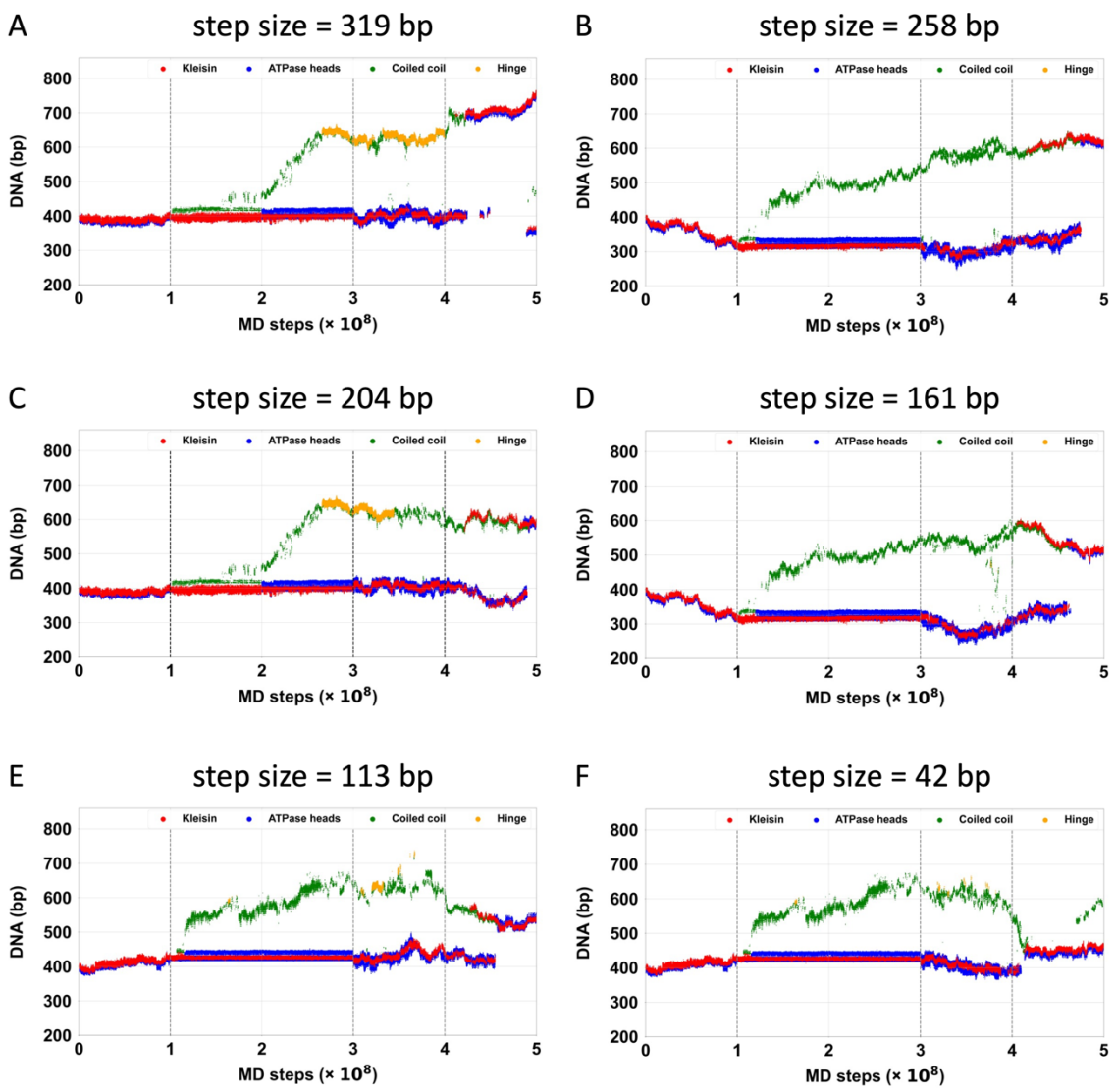

Supplementary Figure S7: Time series of the DNA position where each SMC and kleisin domain contacts. DNA-Protein contacts at kleisin, ATPase heads, coiled-coil, and hinge domains are plotted in red, blue, green, and orange, respectively. SMC-ScpA complex realizes a variety of step sizes such as (A) 310 bp, (B) 258 bp, (C) 204 bp, (D) 161 bp, (E)113 bp, and (F) 42 bp.

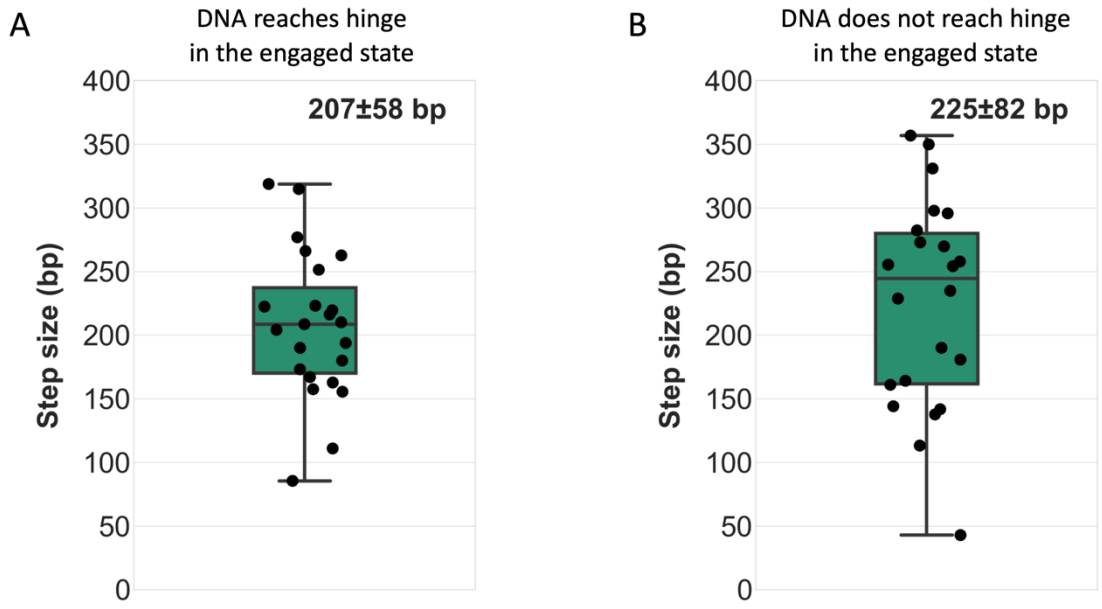

Supplementary Figure S8: Translocation step size for (A) trajectories in which the DNA reaches the hinge domain and for (B) trajectories in which the DNA does not reach the hinge in the engaged state.

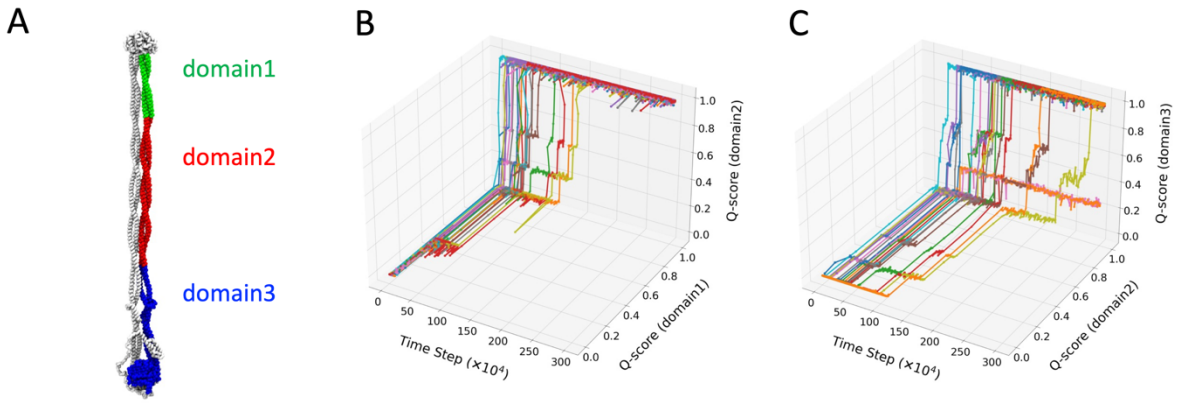

Supplementary Figure S9: Zipping up the coiled-coil arms when transition from V-shape to disengaged states. (A) The definition domains where the coiled-coil arm and ATPase heads are divided into three domains. (B) Time series of Q scores for domain 1 and domain 2 for all simulations. (B) Time series of Q scores for domain 2 and domain 3 for all simulations.

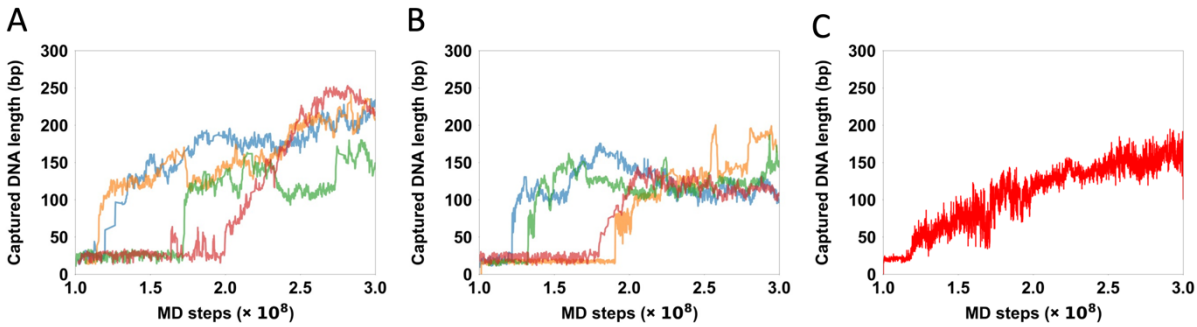

Supplementary Figure S10: Time series of the captured DNA length within the SMC ring in the engaged state during t = 1.0×10^8 - 3.0×10^8 MD steps. (A) Captured DNA length for the trajectories that lead to the DNA translocation successfully in the subsequent states. (B) Captured DNA length for the trajectories that do not lead to the DNA translocation in the subsequent states. (C) Time series of the averaged captured DNA length.

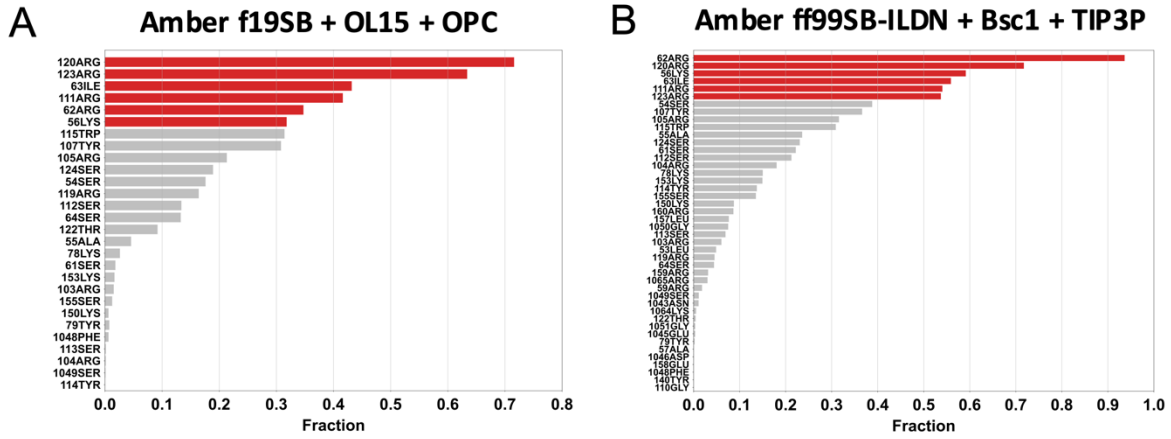

Supplementary Figure S11: Force field dependence of tendency of hydrogen bond formation between SMC ATPase heads and DNA. (A) Fraction of hydrogen bond using Amber ff19SB for protein, OL15 for DNA, and OPC model for water. (B) Fraction of hydrogen bond using Amber ff99SB-ILDN for protein, Bsc1 for DNA, and TIP3P model for water. Although there were variations in the fractions and rankings, the top six amino acid residues that form hydrogen bonds with DNA were common in both force field parameter sets: 120Arg, 123Arg, 63Ile, 111Arg, 62Arg, and 56Lys. Even in amino acid residues with a lower fraction of hydrogen bond formation, we found common amino acid residues between two force field parameter sets such as 115Trp, 107Tyr 105Arg, 124Ser, 54Ser, and so forth. Therefore, the choice of force field and water models has only a minor impact on the hydrogen bond formation pattern between the SMC ATPase heads and DNA.

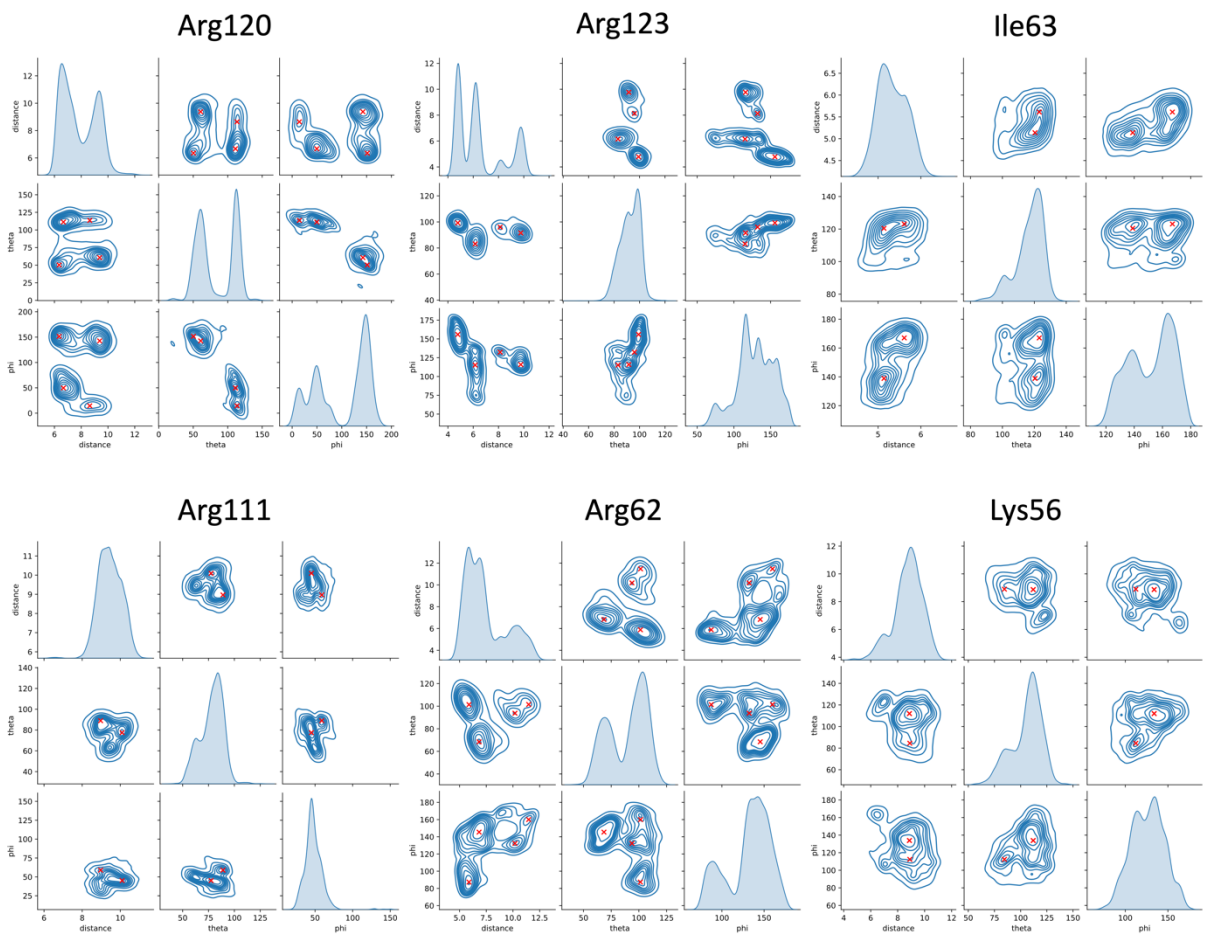

Supplementary Figure S12: Probability distribution of the coarse-grained hydrogen bond parameters, *r*, *θ*, and *φ* for frequently hydrogen-bond forming residues. The red points are optimized hydrogen-bond parameters, which corresponding to peak positions.